Date	Chapter	Speaker
5/12	16/20	Ya-Chien
5/19	16	Aravind Bo Yao
5/26	19 20	Paul Zhi-Ren
6/2	9 22	Fu-Kuo Dronyak
6/9	13 14/24 26	Bo-Haung Shiung Ja-Yeh

Chapter 26
SPR/SERS

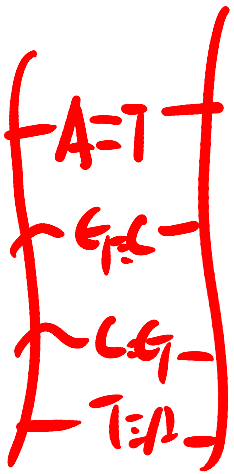

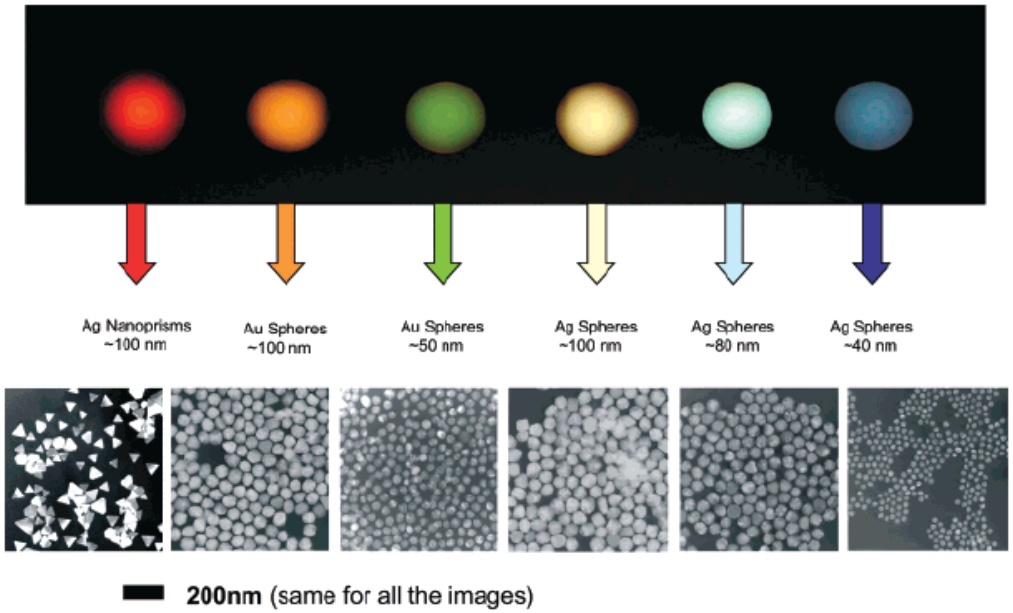

Figure 1. Sizes, shapes, and compositions of metal nanoparticles can be systematically varied to produce materials with distinct light-scattering properties.

Shape-Controlled Synthesis and Surface Plasmonic Properties of Metallic Nanostructures

$\gamma_{111} < \gamma_{100} < \gamma_{110}$

MRS BULLETIN • VOLUME 30 • MAY 2005

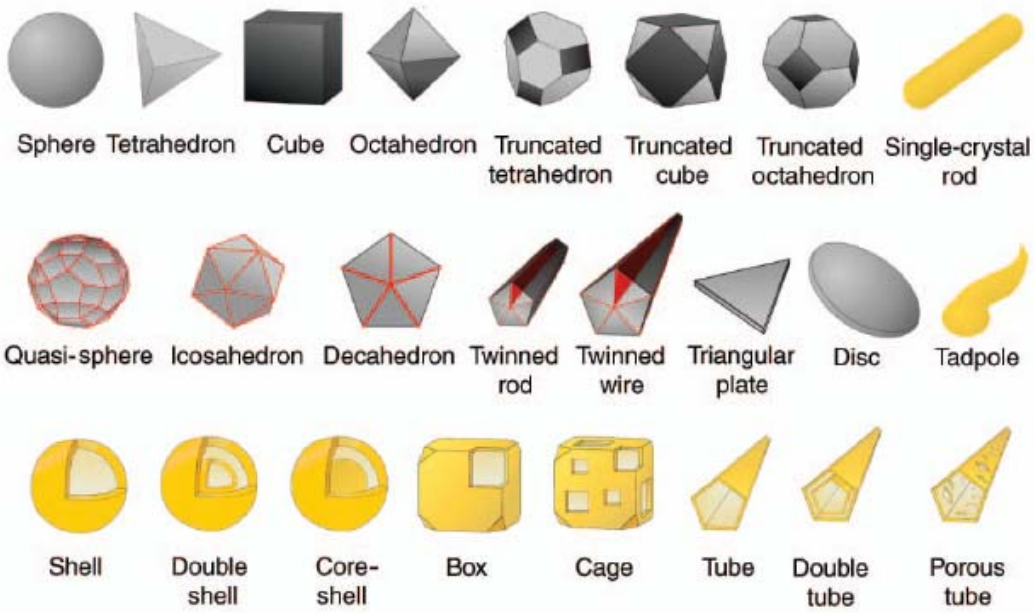

Figure 1. Schematic illustration of nanostructure shapes. The shapes in the top row are single crystals, in the second row are particles with twin defects or stacking faults, and in the third row are gold shells. All twinned and single-crystal shapes shown, with the exception of the octahedron, can be synthesized in solution. Control of shape allows control of optical and catalytic properties, as well as suitability for electronic applications in the case of wires, tubes, and possibly rods. Dark facets are (100) planes, light gray are (111) planes, and {111} twin planes are shown in red. Gold shapes represent gold particles, and gray shapes represent silver particles, although spheres, twinned rods, icosahedrons, and cubes can also be made from gold.

For a bulk metal with infinite sizes in all three dimensions, ω_p can be expressed as

$$\omega_p = (Ne^2/\varepsilon_0 m_e)^{1/2}, \quad (1)$$

where N is the number density of electrons, ε_0 is the dielectric constant of a vacuum, and e and m_e are the charge and effective mass of an electron, respectively. Quantized plasma oscillations are called *plasmons*.

$(1\cdot1\cdot1)(1\cdot1\cdot1)$
$= \sqrt{3}\cdot\sqrt{3}\cos\theta$

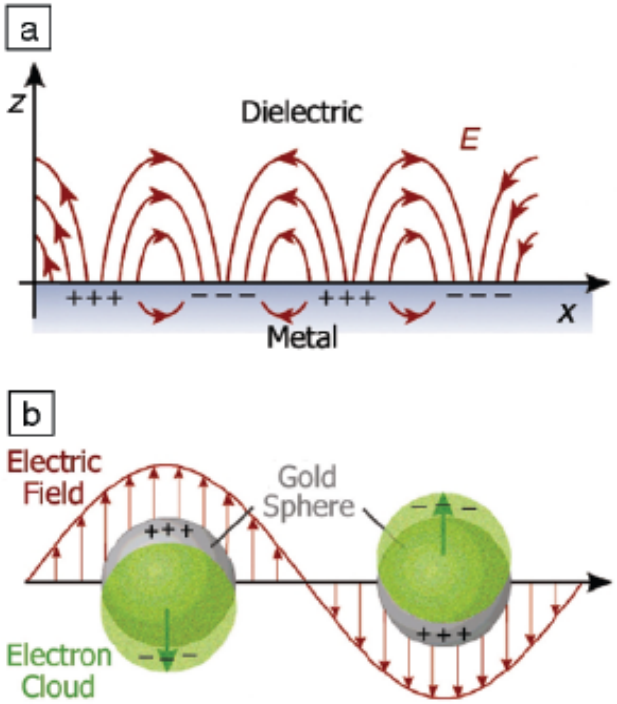

Figure 2. Schematic illustration of the collective oscillations of free electrons for (a) a metal–dielectric interface and (b) a spherical gold colloid. Excited by the electric field of incident light, the free electrons can be collectively displaced from the lattice of positive ions (consisting of nuclei and core electrons). While the plasmon shown in (a) can propagate across the surface as a charge density wave, the plasmon depicted in (b) is localized to each particle. (Courtesy of R. Van Duyne and T. Schatz, Northwestern University.)

Thin film
Nanoparticle
Nanoparticle array

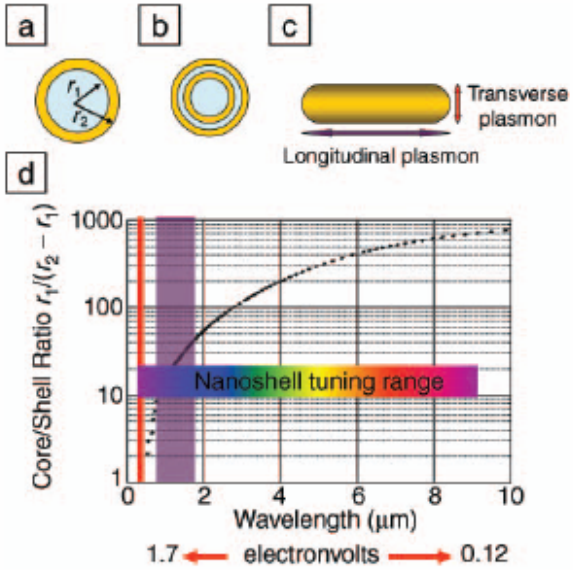

Figure 1. (a) Schematic illustration of a silica-core, gold-shell nanoshell, indicating inner (r_1) and outer (r_2) radii of the shell layers. (b) Depiction of a four-layer, concentric nanoshell. (c) Schematic illustration of a metallic nanorod. (d) Plot of nanoshell resonance as a function of core and shell dimensions, overlaid with reported spectral ranges of nanorod resonances (red, transverse plasmon; purple, longitudinal plasmon), and reported nanoshell and concentric nanoshell combined spectral range of plasmon response.

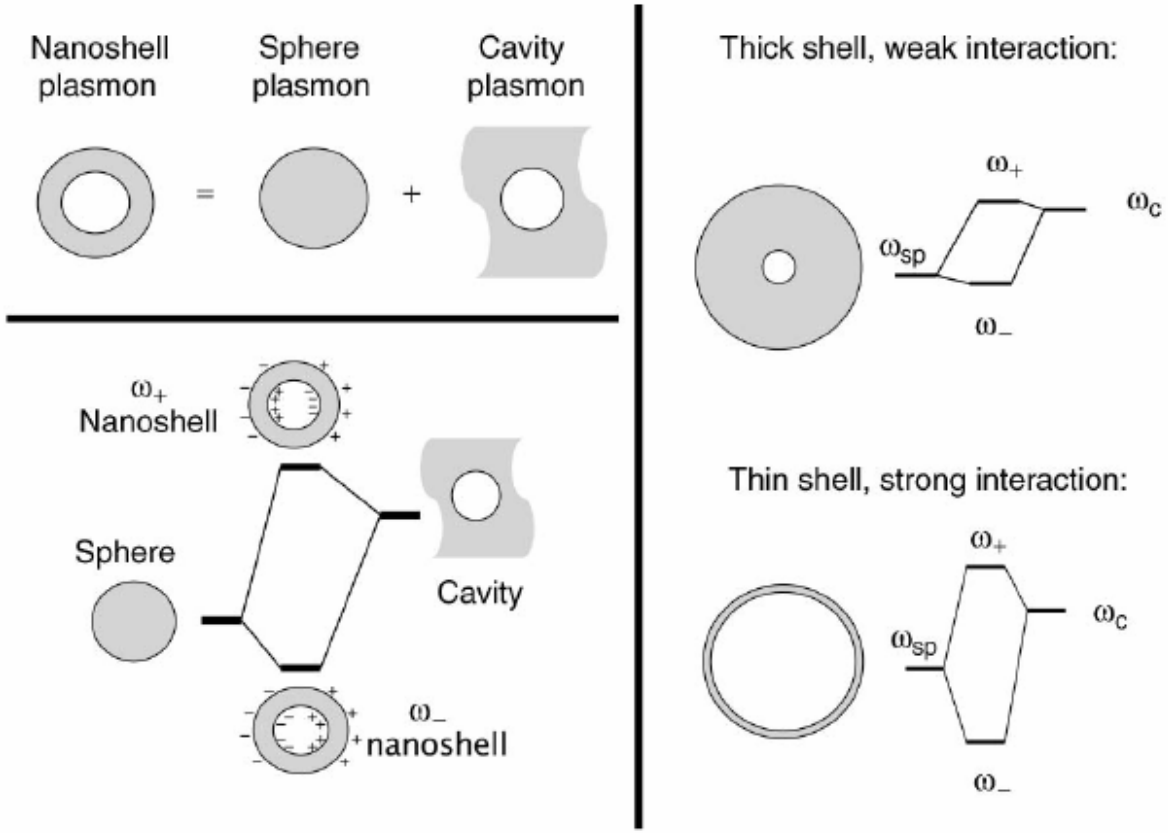

Figure 2. Plasmon hybridization and the sphere–cavity model for nanoshells: the interaction between a sphere (resonance frequency, ω_{sp}) and a cavity plasmon (resonance frequency, ω_c) is tuned by varying the thickness of the shell layer of the nanoparticle. Two hybrid plasmon resonances, the ω_- "bright," or "bonding," plasmon and the ω_+ "dark," or "anti-bonding," plasmon resonances are formed. The lower-energy plasmon couples most strongly to the optical field.

$\frac{10^{10} - 10^{4}}{10^{10}} \sim 1$

$I_0 \times e^{-6} \times Q.E$

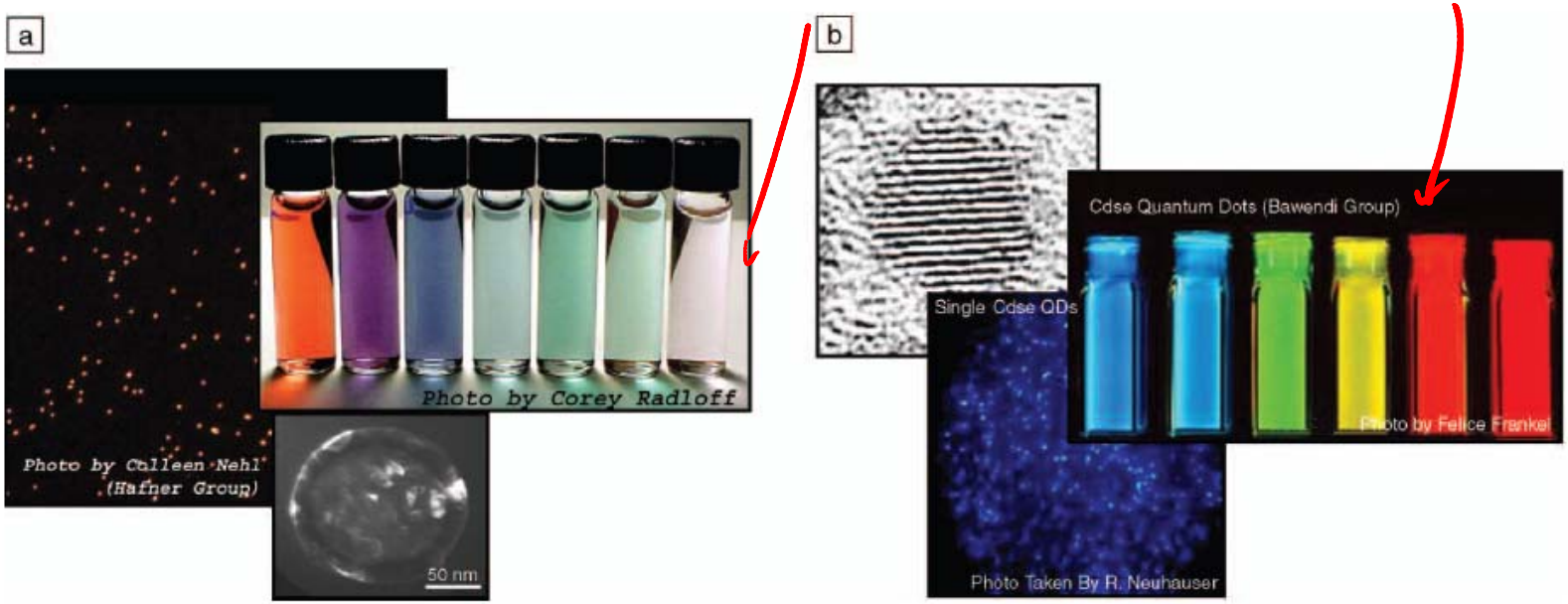

Figure 3. (a) Nanoshells are tunable plasmonic nanoparticles. Micrographs show a field of many nanoshells (large micrograph) and one nanoshell (small micrograph). Vials show nanoshells in solution. (b) Semiconductor quantum dots are tunable excitonic nanoparticles (courtesy of the Bawendi group). A field of quantum dots is displayed in the bottom image; an individual quantum dot is shown in the upper-left micrograph. Vials of quantum dots are also shown. Comparing single nanoshells to single quantum dots, nanoshells typically have a 10^6 larger absorption cross section, nominally five times the physical cross section of the nanoparticle.

10^{10}

$10^{11} \times 10^{-5} = 10^{5}$

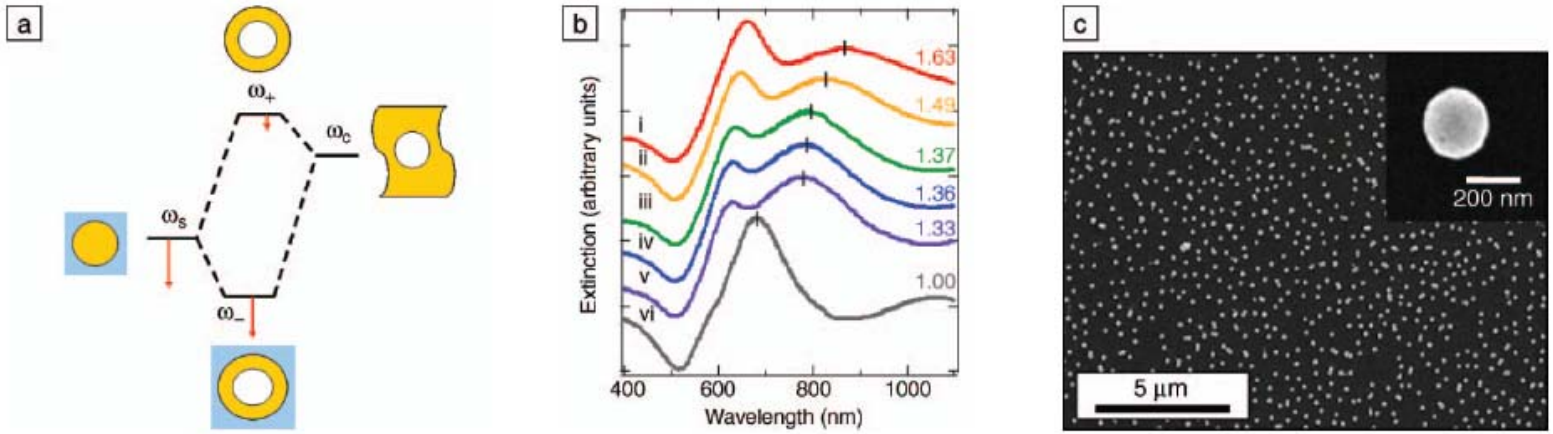

Figure 5. (a) Plasmon hybridization picture applied to surface plasmon resonance sensing with nanoshells: the low-energy "bonding" plasmon, ω_-, is sensitized to changes in its dielectric environment. The blue background schematically denotes the embedding medium for the nanoparticle. (b) Experimental curves showing plasmon resonance shifts for nanoshell-coated films in various media: (i) carbon disulfide, (ii) toluene, (iii) hexane, (iv) ethanol, (v) H_2O, and (vi) air. The index of refraction for each embedding medium is noted on the far right of the spectra. Spectra are offset for clarity. (c) Scanning electron micrograph of nanoshells deposited onto a poly(vinyl pyridine) functionalized glass surface, as used to acquire data in (b). Inset: individual nanoshell.

Far-Field Optical Microscopy of Single Metal Nanoparticles

Acc. Chem. Res. **2005**, *38*, 594–601

The optical properties of metals are, to a large extent, determined by conduction electrons. The response of these free electrons follows the Drude model. They collectively react to perturbation by an external electric field. The Coulomb restoring force between the electrons and the lattice leads to harmonic oscillations with the plasma frequency $\omega_p^2 = Ne^2/(m_e\epsilon_0)$ where N is the electron density and m_e the electron mass. The damping of the oscillation is described by a phenomenological damping constant, γ. In this model, the dielectric function, $\epsilon(\omega)$, equals

$$\epsilon(\omega) = 1 - \frac{\omega_p^2}{\omega(\omega + i\gamma)}$$

For noble metals, the contribution of the bound d-electrons to the optical properties cannot be neglected.[9]

$\varepsilon = \varepsilon' + i\varepsilon''$

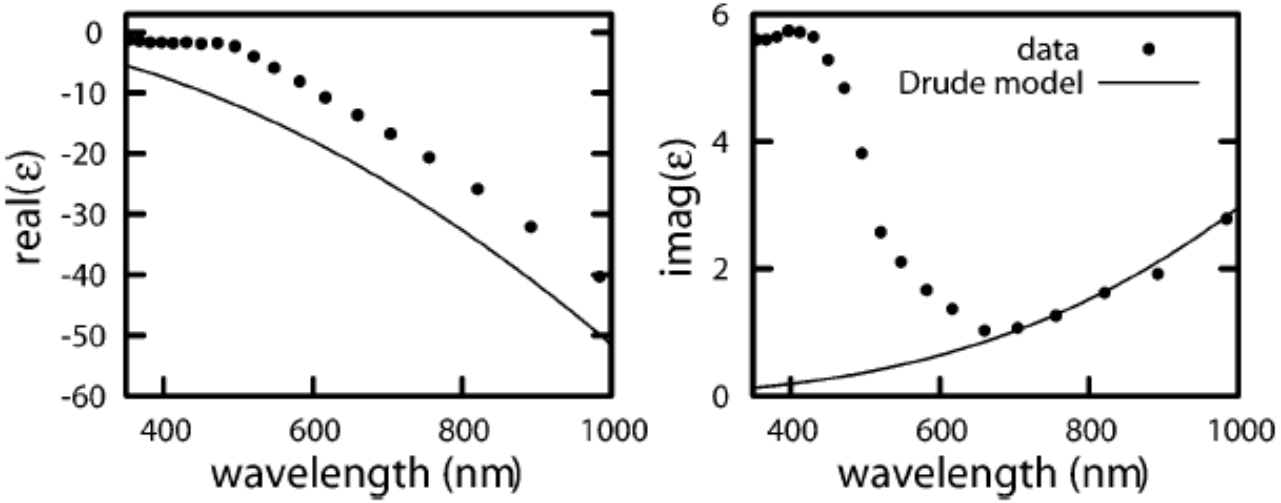

FIGURE 1. Dielectric function of gold[8] compared with the free electron model of Drude. The deviations are due to the interband contribution.

$$\sigma_{\text{ext}} = \sigma_{\text{abs}} + \sigma_{\text{sca}}.$$

$\chi = \frac{\phi}{\lambda}$ Mie's theory

$$\sigma_{\text{ext}} = 2\frac{2\pi}{k^2}x^3\,\text{Im}\left(\frac{m^2-1}{m^2+2}\right)$$

$$m^2 = \frac{\epsilon_{\text{metal}}}{\epsilon_{\text{medium}}} \qquad -2$$

$$\sigma_{\text{sca}} = \frac{4}{3}\frac{2\pi}{k^2}x^6\left|\frac{m^2-1}{m^2+2}\right|^2$$

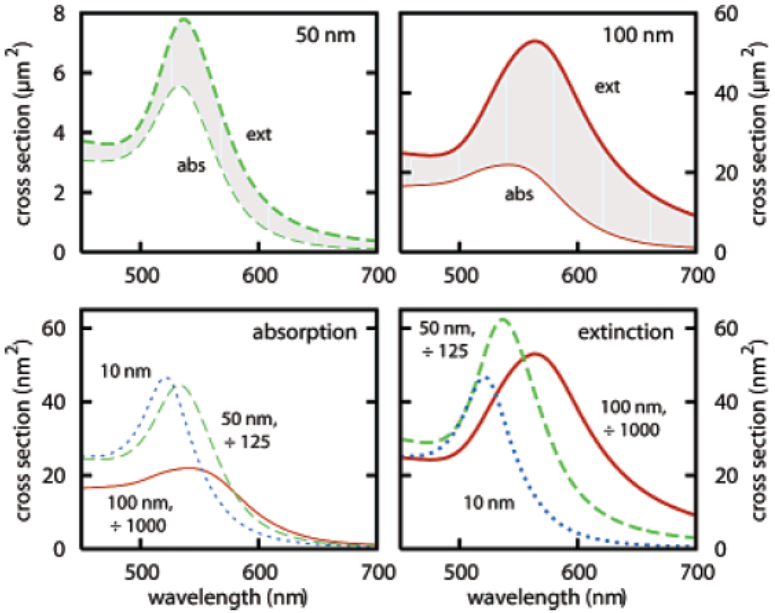

FIGURE 2. Extinction (thick lines) and absorption (thin lines) spectra of gold particles with a diameter of 10 nm (blue, dotted), 50 nm (green, dashed), and 100 nm (red, solid) plotted in different combinations of the same curves. The surrounding medium is water ($n = 1.3$). In the top panels, with increasing colloid size the additional scattering contribution to the extinction becomes more important; the gap between absorption and scattering spectra gets larger. In the bottom panels to compare colloids of different sizes the spectra are scaled with d^3 to the 10-nm particle. Both absorption and scattering spectra show a red shift and broadening of the plasmon resonance with particle size.

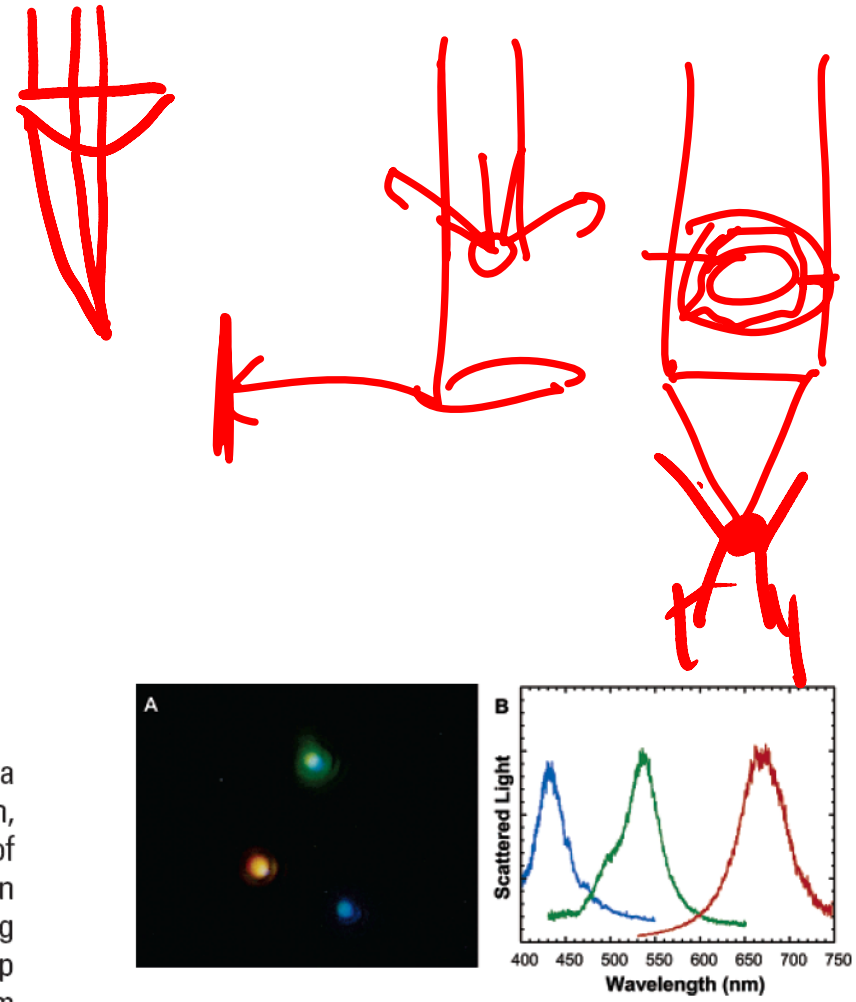

FIGURE 3. Dark-field image of silver particles of different sizes leading to different colors in the scattered white light.[15] The spot size is about 400 nm, and the height of the image is about 9 μm. The corresponding spectra are shown in the right panel. Reprinted with permission from ref 15. Copyright 2000 National Academy of Sciences, U.S.A.

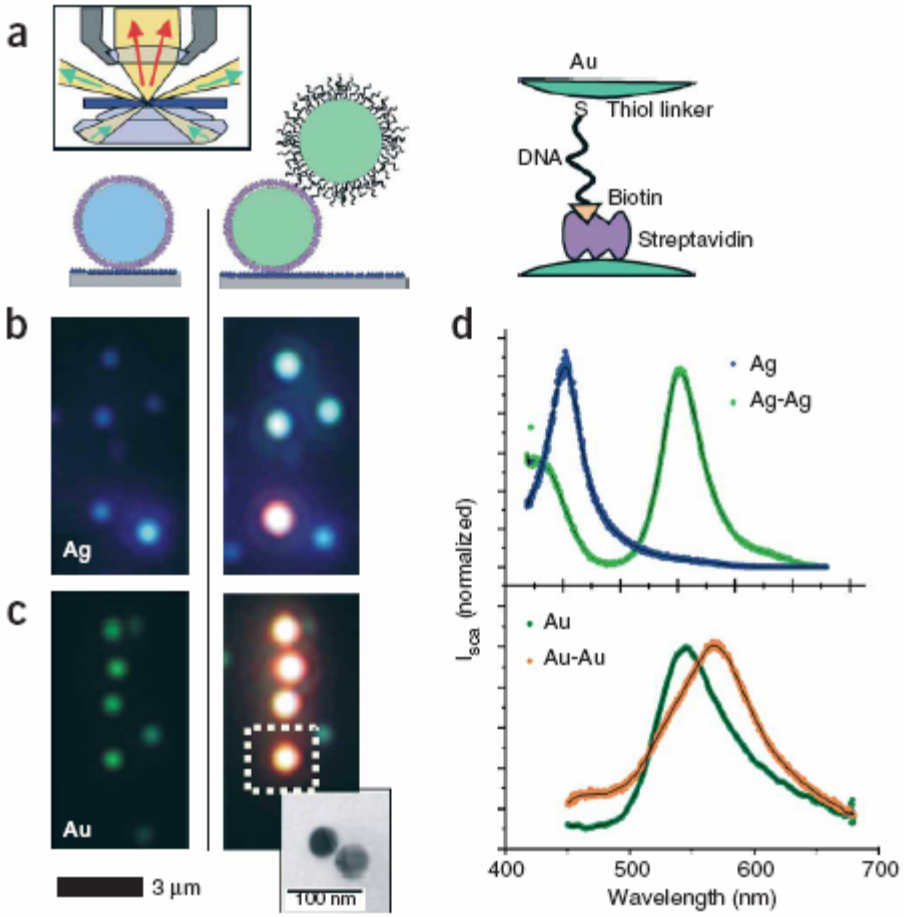

Figure 1 Color effect on directed assembly of DNA-functionalized gold and silver nanoparticles. (**a**) First, nanoparticles functionalized with streptavidin are attached to the glass surface coated with BSA-biotin (left). Then, a second particle is attached to the first particle (center), again via biotin-streptavidin binding (right). The biotin on the second particle is covalently linked to the 3′ end of a 33 base pair long ssDNA strand bound to the particle via a thiol group at the 5′ end. Inset: principle of transmission darkfield microscopy. (**b**) Single silver particles appear blue (left) and particle pairs blue-green (right). The orange dot in the bottom comes from an aggregate of more than two particles. (**c**) Single gold particles appear green (left), gold particle pairs, orange (right). Inset: representative transmission electron microscopy image of a particle pair to show that each colored dot comes from light scatted from two closely lying particles, which cannot be separated optically. (**d**) Representative scattering spectra of single particles and particle pairs for silver (top) and gold (bottom). Silver particles show a larger spectral shift (102 nm) than gold particles (23 nm), stronger light scattering and a smaller plasmon line width. Gold, however, is chemically more stable and is more easily conjugated to biomolecules via –SH, –NH2 or –CN functional groups.

should increase the electrostatic repulsion between the charged gold particles[26]. Consistent with this model, a blue-shift in the spectrum of individual nanoparticle pairs occurred when we decreased the salt concentration of our buffer (normally 0.1 M NaCl) to 0.005 M NaCl (Fig. 2a). When we restored the ionic concentration to the original

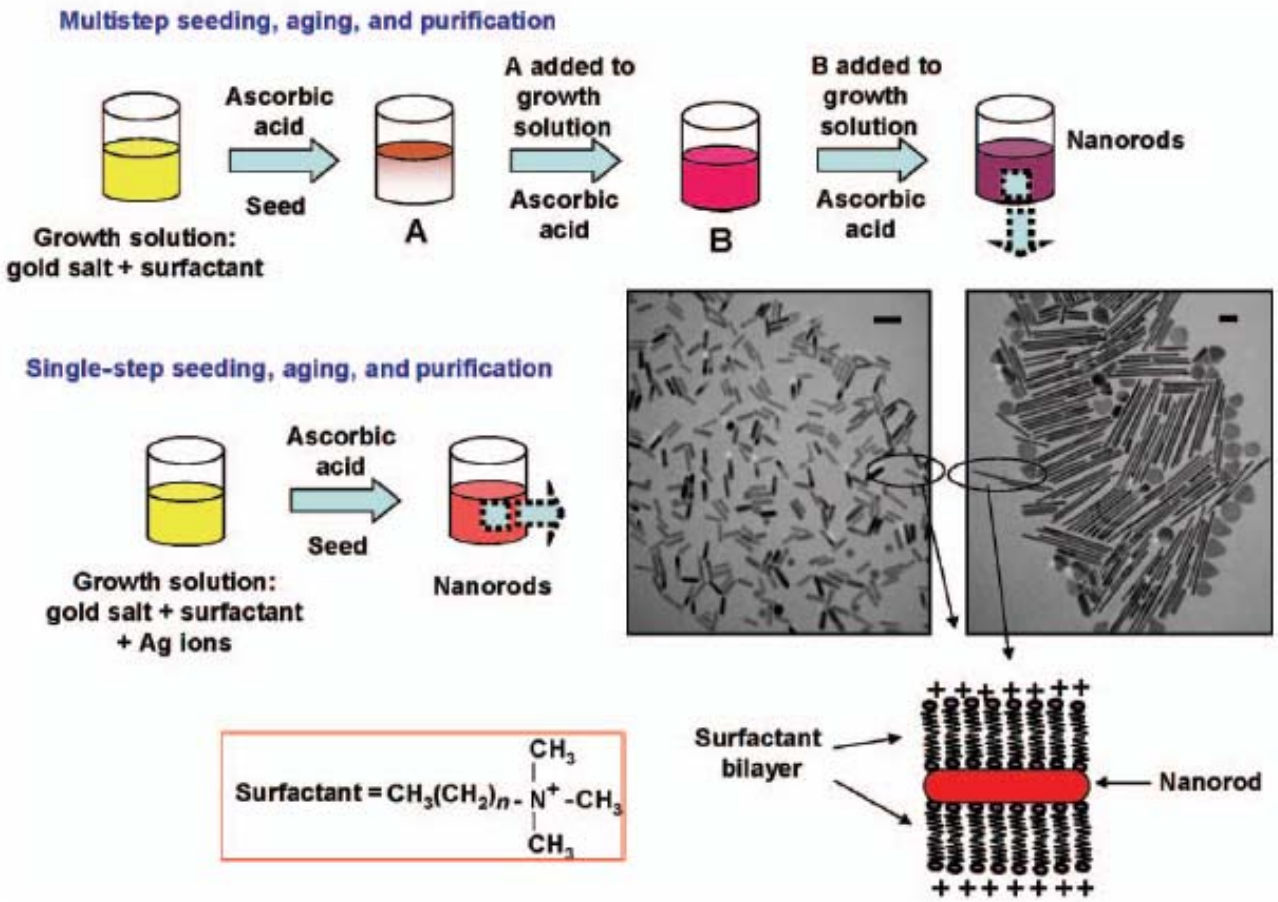

Figure 1. Schematic illustration showing the general methodology for generating gold nanorods by the seeding method. Scale bars in the transmission electron micrographs represent 100 nm.

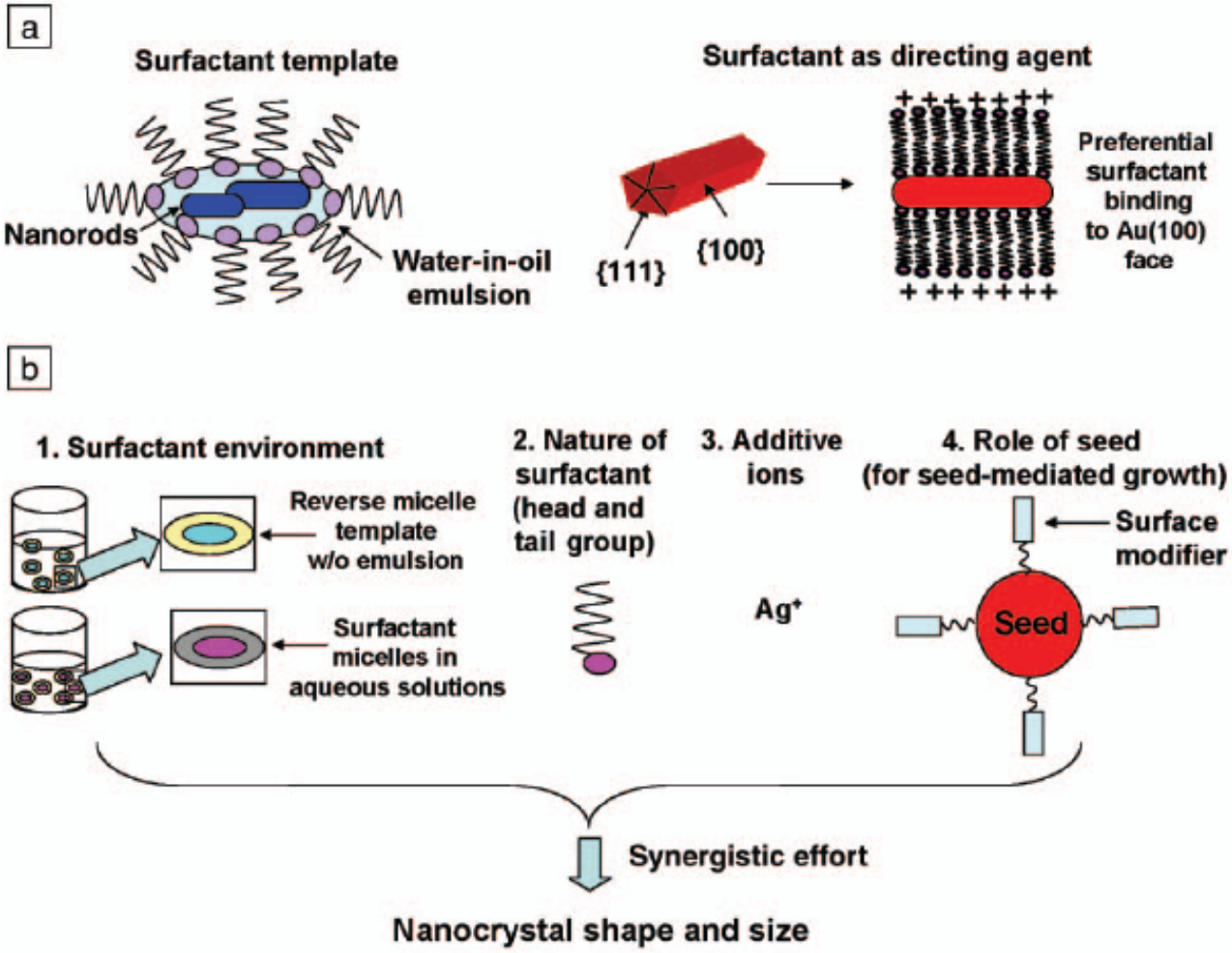

Figure 2. (a) Schematic illustration displaying the different ways in which surfactants can direct the growth of nanorods. (b) Schematic showing various synthetic parameters affecting overall nanocrystal shape and size.

Table I: Summary of Dimensions and Yields for Nanorods and Nanowires.

Methodology Used	Length × Width of Nanorods and Nanowires	Surfactant(s) Used	Remarks	Ref.
Photochemical	Gold nanorods/nanowires: 50 nm–several μm × 15–100 nm	C_{16}TAC	Significant fraction of spherical particles present	21
	Gold nanorods: 50 nm × 18 nm 53 nm × 15 nm 61 nm × 13 nm	C_{16}TAB + TDAB	Very high yield	22
Electrochemical	Gold nanorods: 18–52 nm × 10 nm	C_{16}TAB + TOAB or TDAB	A small fraction of spherical particles present	19, 20
Chemical: aqueous & seeding	Gold nanorods: 74–288 nm × 16 nm 150–600 nm × 25–30 nm	CTAB	Significant fraction of spherical particles present	14, 35
	Gold nanorods: 42–120 nm × 6–12 nm	CTAB + BDAC	Very high yield	17
	Gold nanorods: 87 nm × 42 nm 64 nm × 24 nm 50 nm × 15 nm	CTAB	>90%	27
	Silver nanowires: 1–4 μm × 20–30 nm Silver nanorods: 42–180 nm × 12–20 nm	CTAB	Significant fraction of spherical particles present	15
Chemical: water-in-oil & non-seeding	Copper nanowires/nanorods: several nm–1 μm × several nm	AOT, Cu-$(AOT)_2$	Significant fraction of spherical particles present	28, 29

Notes: C_{16}TAC = cetyltrimethylammonium chloride; C_{16}TAB, CTAB = cetyltrimethylammonium bromide; TDAB = tetradecylammonium bromide; TOAB = tetraoctylammonium bromide; BDAC = benzyldimethylhexadecylammonium chloride; AOT = aerosol-OT, chemical name, sodium bis(2-ethylhexyl)sulfosuccinate.

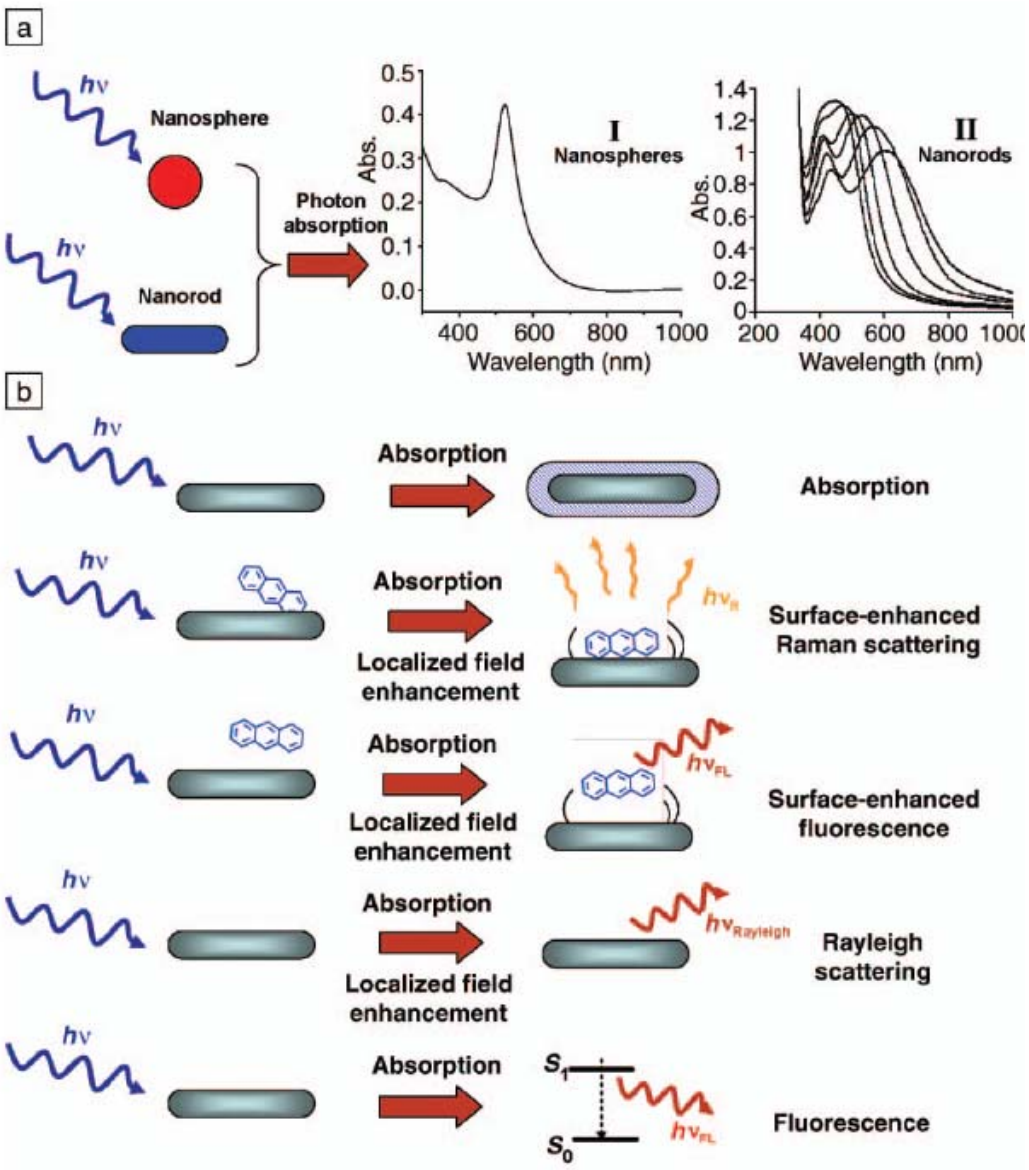

Figure 3. (a) Schematic illustration showing the shape-dependent optical properties of gold nanospheres (I) and silver nanorods of aspect ratios 1–10 (II). (b) Schematic showing the general optoelectronic behavior of anisotropic materials. Photons are indicated by hν.

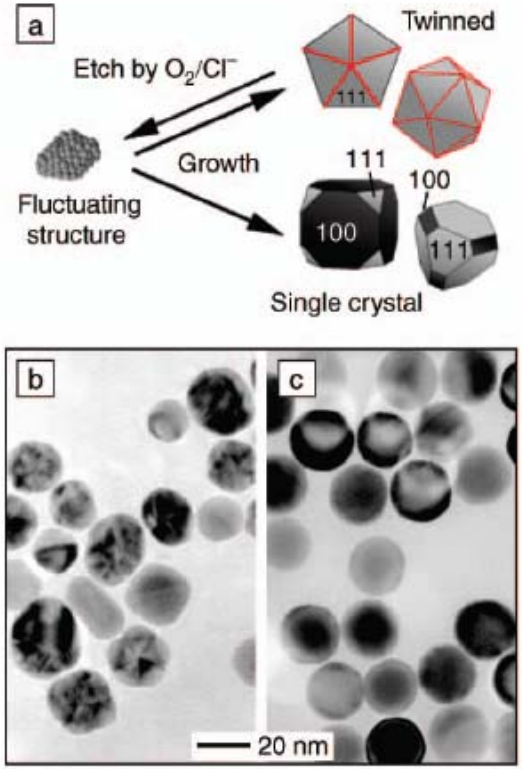

Figure 1. (a) Schematic illustration of the mechanism by which high yields of single-crystalline seeds were obtained. The {111} facets, {100} facets, and {111} twin planes are shown in light grey, dark grey, and red, respectively. Other twinned particles besides the decahedron and icosahedron may also be present in the reaction. (b) Transmission electron microscopy (TEM) image of a mixture of twinned seeds (with a heterogeneous contrast under TEM) and single-crystalline seeds (with a homogeneous contrast) produced at t *= 4 min when no chloride was introduced. (c) When 0.06 mM chloride was added to the same synthesis, a second round of nucleation took place at* t *= 24 h, resulting in high yields of single-crystalline seeds at* t *= 44 h.*

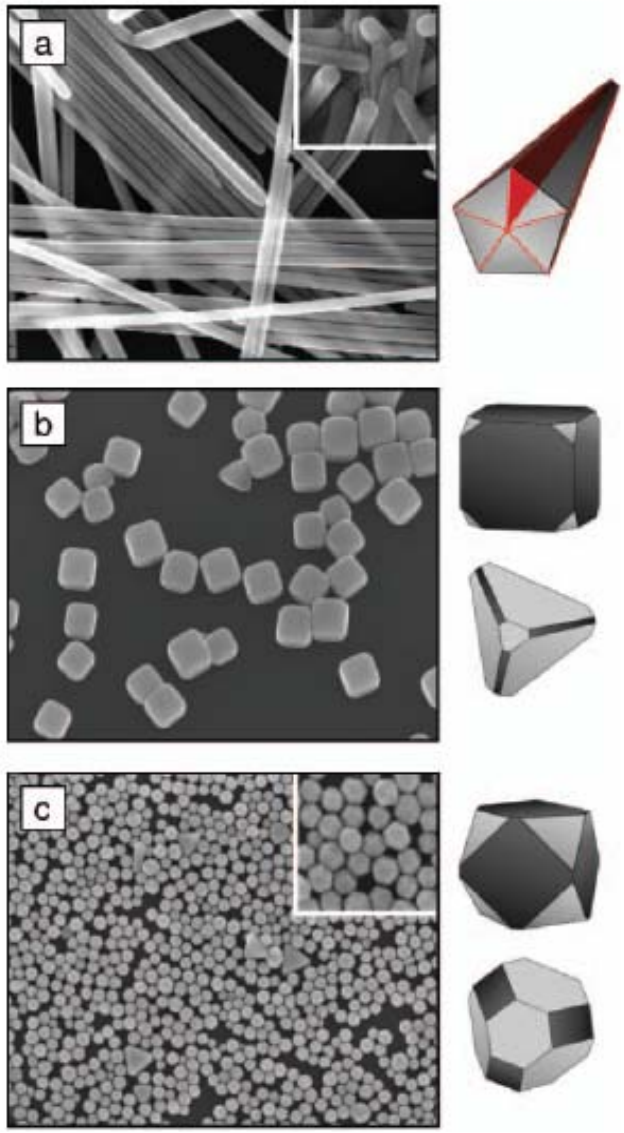

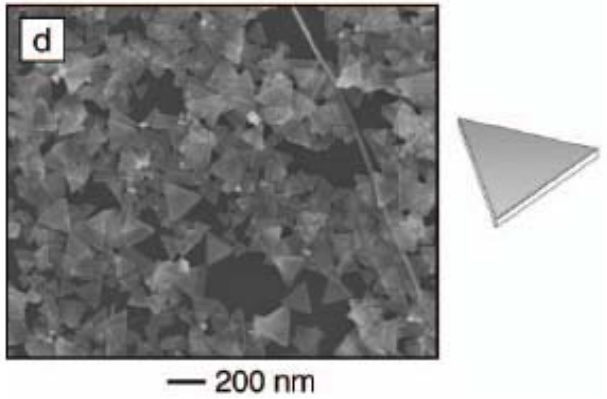

Figure 2. Scanning electron microscopy (SEM) images of representative silver nanostructures: (a) wires, (b) cubes, (c) truncated cubes and tetrahedra, and (d) triangular plates, all at the same scale. Insets show high-magnification SEM images of these nanostructures. In the schematic illustrations to the right of each micrograph, the {111} facets, {100} facets, and {111} twin planes are shown in light grey, dark grey, and red, respectively. The side surfaces of each triangular nanoplate should contain a mixture of low-index planes, but are left blank here, since their exact composition is not clear.

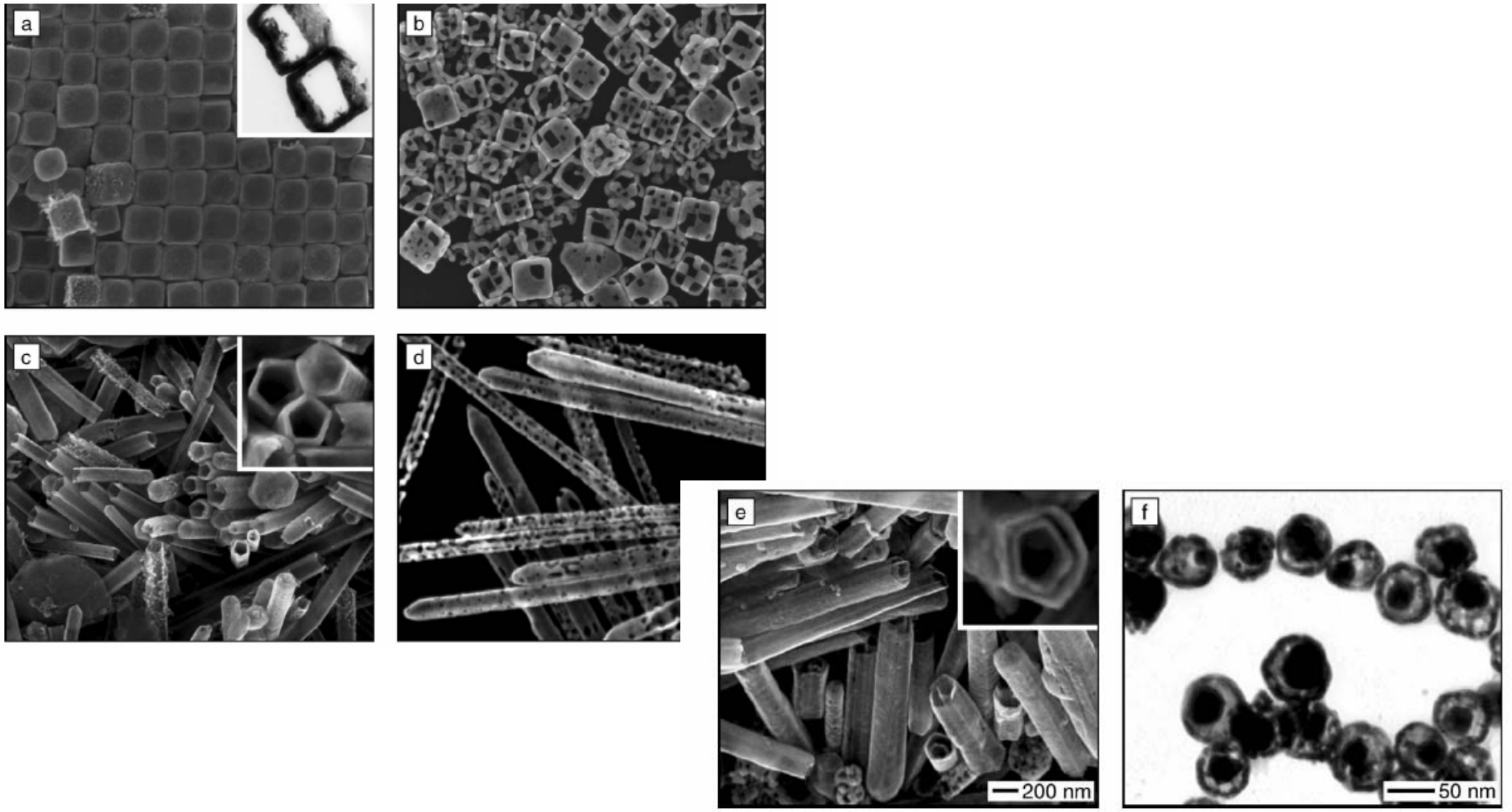

Figure 3. (a) Scanning electron microscopy (SEM) image of Au/Ag alloyed nanoboxes synthesized by reacting Ag nanocubes with $HAuCl_4$ in an aqueous medium. The inset shows a transmission electron microscopy (TEM) image of two microtomed boxes, confirming their hollow structure. (b) Addition of more $HAuCl_4$ induced the dealloying of silver from the walls and the formation of pinholes. (c), (d) Alloying and dealloying were also observed when silver nanowires served as the template. Note the hollow interior matching the pentagonal cross section of the nanowire. (e), (f) SEM and TEM images of double-walled nanotubes and nanorattles of Au/Ag alloys that were produced by combining the galvanic replacement reaction with the electroless plating of silver. The SEM images in (a)–(e) are at the same scale, as shown by the scale marker in (e); the scale of (f) is noted in the micrograph.

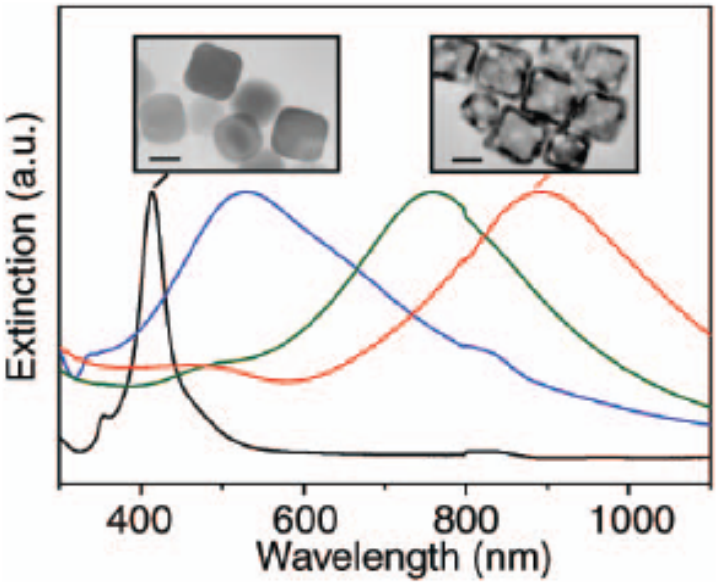

Figure 4. Transformation of 30 nm Ag nanocubes into Au/Ag alloyed nanoboxes and nanocages resulted in a continuous shift of their surface plasmon resonance (SPR) peak from 400 nm to 900 nm, which is in the transparent window of biological tissue. The SPR peak position is determined by the molar ratio between $HAuCl_4$ and Ag involved in the replacement reaction. Insets show TEM images of the cubes and cages; scale bar in each figure represents 20 nm.

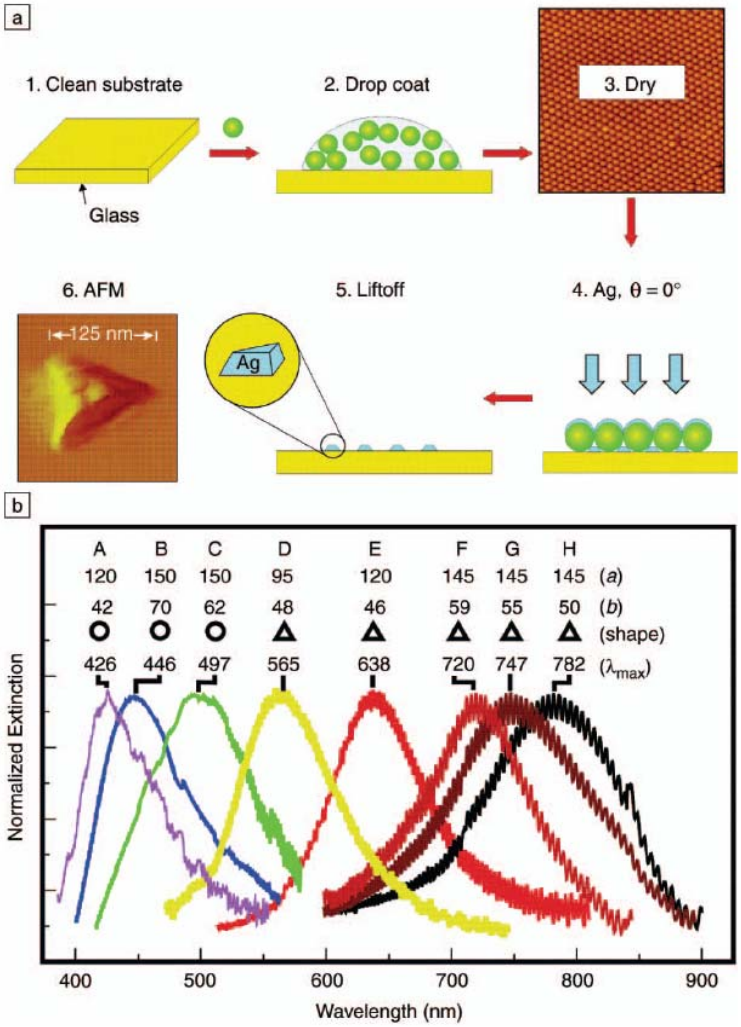

Figure 1. (a) Schematic representation of the nanosphere lithography (NSL) fabrication process. The AFM image in step 3 is 5 μm × 5 μm. (b) Size- and shape-tunable localized surface plasmon resonance spectra of various Ag nanoparticles (labeled A–H) fabricated by NSL. The wavelength of maximum extinction, λ_{max}, is changed by varying the in-plane width a *and out-of-plane height* b *of the nanoparticles.*

The simplest theoretical approach available for modeling the optical properties of nanoparticles is classical electrodynamics (i.e., solving Maxwell's equations with the metal dielectric constant taken from bulk measurements). For spherical particles, this leads to the following (Mie theory) expression for the extinction coefficient $E(\lambda)$ in the long-wavelength limit:[23]

$$E(\lambda) = \frac{24\pi N_A a^3 \varepsilon_m^{3/2}}{\lambda \ln(10)} \times \left[\frac{\varepsilon_i}{(\varepsilon_r + 2\varepsilon_m)^2 + \varepsilon_i^2} \right]. \quad (1)$$

Here, N_A is the areal density of the nanoparticles, a is the radius of the metallic nanosphere, ε_m is the dielectric constant of the medium surrounding the nanosphere (assumed to be a positive, real number), λ is the wavelength, and ε_r and ε_i are the real and imaginary parts of the metal dielectric function. This formula predicts a resonant peak when $\varepsilon_r = -2\varepsilon_m$, which for silver and gold occurs in the visible portion of the spectrum. In addition, any change in the dielectric constant of the medium (e.g., when molecules adsorb on the particle) leads to a change in the resonance wavelength.

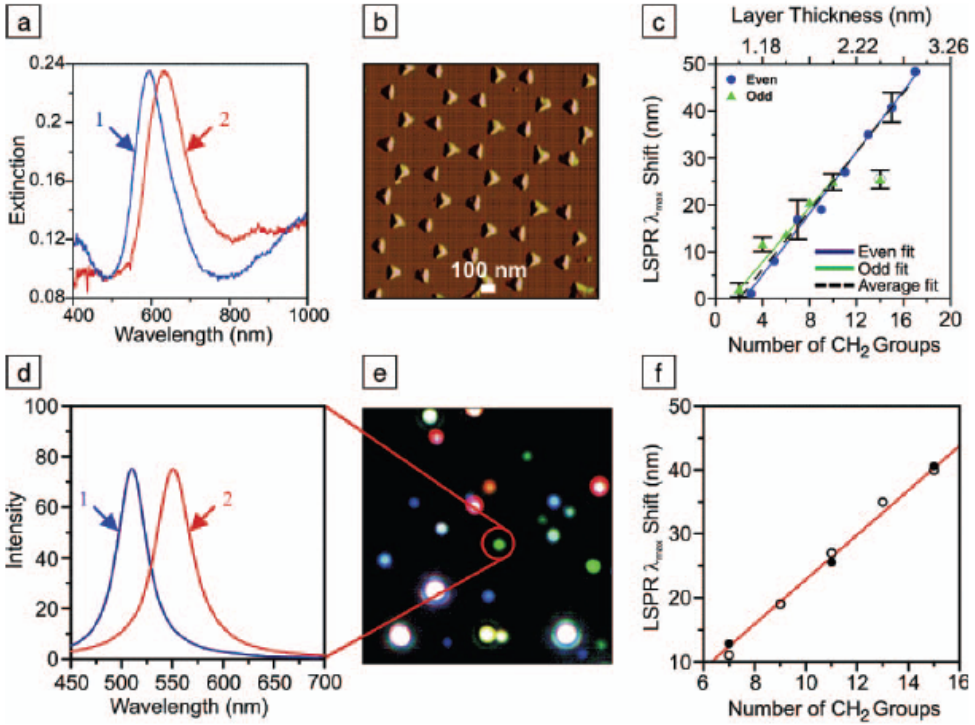

Figure 3. (top row) Localized surface plasmon resonance (LSPR) spectroscopy of a Ag nanoparticle array fabricated by nanosphere lithography in a N_2 environment: (a) Extinction spectrum of the array (curve 1) before chemical modification, wavelength of extinction maximum λ_{max} = 594.8 nm, and (curve 2) after modification with 1 mM hexadecanethiol, λ_{max} = 634.8 nm. (b) Tapping-mode atomic force microscopy (AFM) image of the array in (a); nanosphere diameter D = 390 nm, deposited mass thickness d_m = 50 nm; Ag on mica substrate; scan area, 3.0 μm^2. After solvent annealing, nanoparticle in-plane width is 100 nm and out-of-plane height is 51 nm. (c) Alkanethiol chain length dependence on the LSPR spectral peak shifts for the array. Even and odd carbon chain lengths are depicted with different symbols to emphasize the difference in the terminal bond orientation with respect to the substrate, which leads to different observed trends for the two cases. (bottom row) LSPR spectroscopy of single Ag nanoparticles produced by chemical synthesis: (d) scattering spectrum of a single Ag nanoparticle (curve 1) before chemical modification, λ_{max} = 510.2 nm, and (curve 2) after modification with 1 mM hexadecanethiol, λ_{max} = 550.9 nm. The circled nanoparticle in (e) produced the signal for these curves. (e) Dark-field resonant Rayleigh scattering image of a random array of chemically synthesized Ag nanoparticles (image dimensions, 130 $\mu m \times 130 \mu m$). (f) Alkanethiol chain length dependence on the LSPR spectral peak shifts for a single Ag nanoparticle. The open circles represent an overlay of the array data from (c). The solid circles are single nanoparticle measurements.

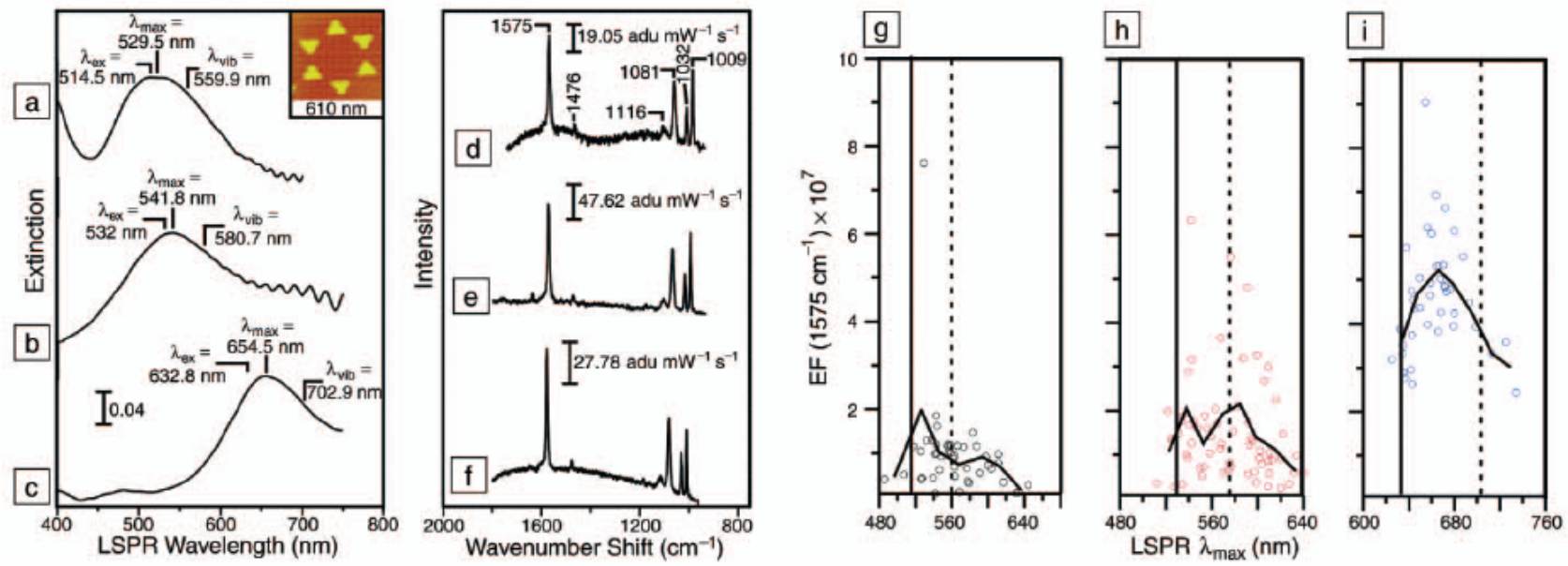

Figure 5. (a)–(f) Correlated, spatially resolved, localized surface plasmon resonance (LSPR) and surface-enhanced Raman spectroscopy (SERS) results for benzenethiol adsorbed on Ag nanoparticle arrays fabricated by nanosphere lithography. (a), (d) Ag nanoparticles fabricated with nanosphere diameter D = *280 nm and deposited mass thickness* d_m = *36 nm, probed with an excitation wavelength* λ_{ex} = *514.5 nm, power = 0.7 mW. A representative atomic force micrograph of the substrate is shown in the inset. (b), (e) Ag nanoparticles fabricated with* D = *280 nm,* d_m = *36 nm, probed with* λ_{ex} = *532.0 nm, power = 0.7 mW. (c), (f) Ag nanoparticles fabricated with* D = *400 nm,* d_m = *56 nm, probed with* λ_{ex} = *632.8 nm, power = 1.2 mW. (g)–(i) Plasmon-sampled surface-enhanced Raman excitation spectroscopy (PS-SERES) results for the 1575 cm^{-1} band of benzenethiol with three different excitation wavelengths: (g)* λ_{ex} = *514.5 nm, (h)* λ_{ex} = *532.0 nm, and (i)* λ_{ex} = *632.8 nm. For each* λ_{ex}, *both the wavelength location of the excitation (solid line) and the scattering (dashed line) are marked. The overlaid curves represent the bin-averaged values of the LSPR* λ_{max} *and the enhancement factor. Bin widths are (g) 24 nm, (h) 16 nm, and (i) 16 nm.*

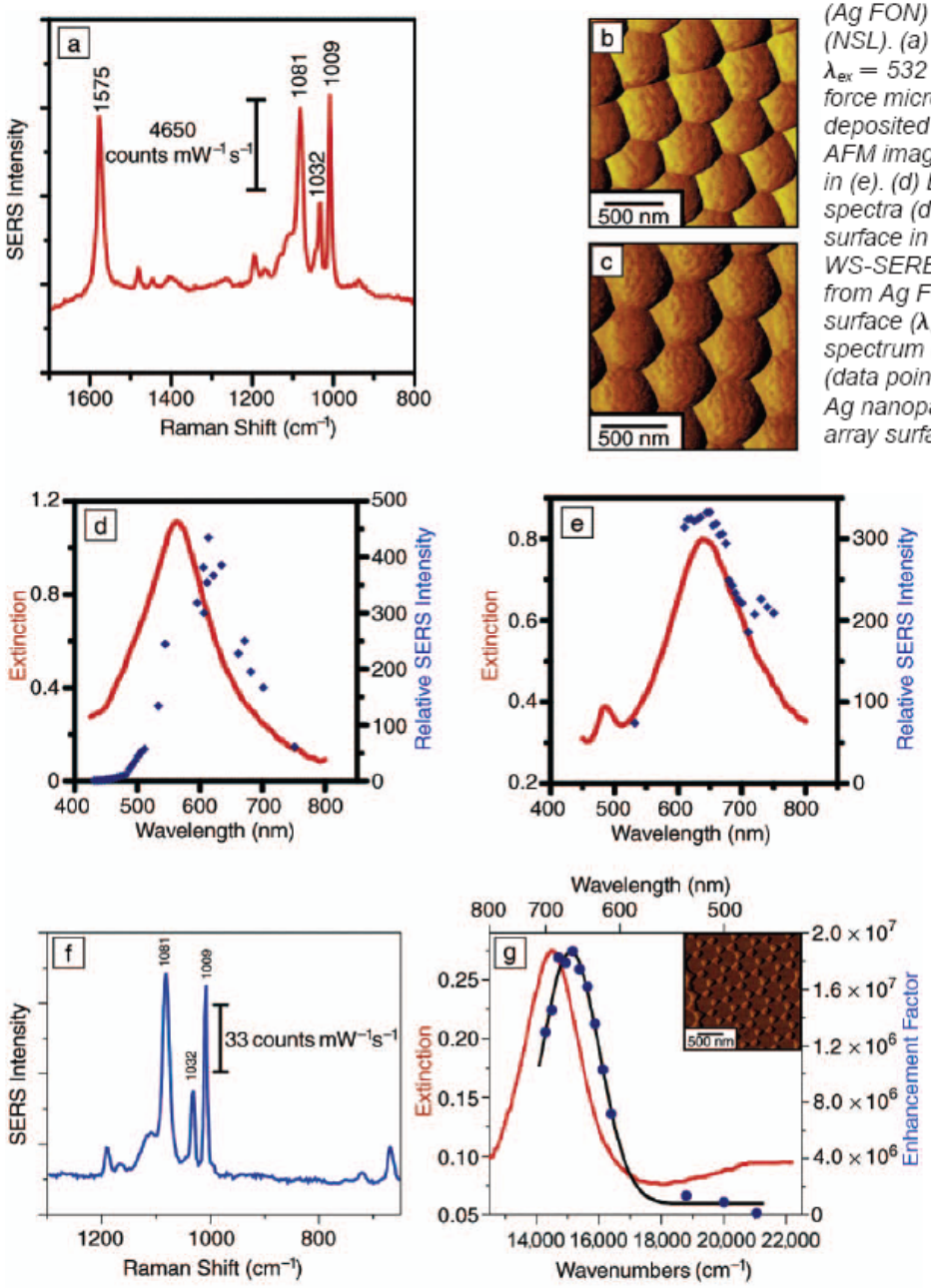

Figure 6. Localized surface plasmon resonance (LSPR), surface-enhanced Raman spectroscopy (SERS), and wavelength-scanned surface-enhanced Raman excitation spectroscopy (WS-SERES) results for benzenethiol adsorbed on Ag film-over-nanosphere (Ag FON) surfaces and nanoparticle arrays fabricated by nanosphere lithography (NSL). (a) SERS spectrum measured from Ag FON surface with excitation wavelength λ_{ex} = 532 nm, power = 3.0 mW, and 100 s data acquisition time. (b) Contact-mode atomic force microscopy (AFM) image of Ag FON surface (nanosphere diameter D = 410 nm, deposited mass thickness d_m = 200 nm) used for SERS in (a). (c) Contact-mode AFM image of Ag FON surface (D = 500 nm, d_m = 250 nm) used for WS-SERES in (e). (d) LSPR spectrum (solid line, λ_{max} = 562 nm, FWHM = 144 nm) and WS-SERES spectra (data points) for the 1081 cm^{-1} band of benzenethiol measured from the Ag FON surface in (b). (e) LSPR spectrum (solid line, λ_{max} = 638 nm, FWHM = 131 nm) and WS-SERES spectra (data points) for the 1081 cm^{-1} band of benzenethiol measured from Ag FON surface in (c). (f) SERS spectrum measured from Ag nanoparticle array surface (λ_{ex} = 532 nm, power = 3.0 mW, 100 s data acquisition time). (g) LSPR spectrum (solid line, λ_{max} = 688 nm, FWHM = 95 nm) and WS-SERES spectra (data points) for the 1081 cm^{-1} band of benzenethiol measured from a Ag nanoparticle array surface. (inset) Tapping-mode AFM image of a representative array surface.

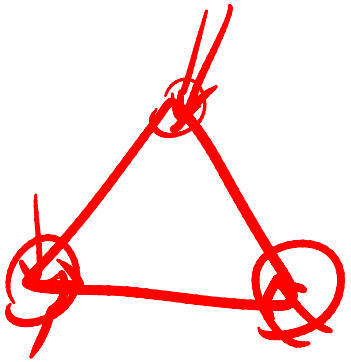

INTERFACES AND THIN FILMS AS SEEN BY BOUND ELECTROMAGNETIC WAVES

Wolfgang Knoll

character of an electromagnetic mode. The component perpendicular to the interface, E_z, however, does not fall to zero abruptly, but decays exponentially with a decay length l which is a function of the angle of incidence

$$l = \frac{\lambda}{2\pi\sqrt{(n \cdot \sin\theta)^2 - 1}}, \quad \theta > \theta_c. \qquad 1.$$

Such an electromagnetic field distribution is called an evanescent wave.

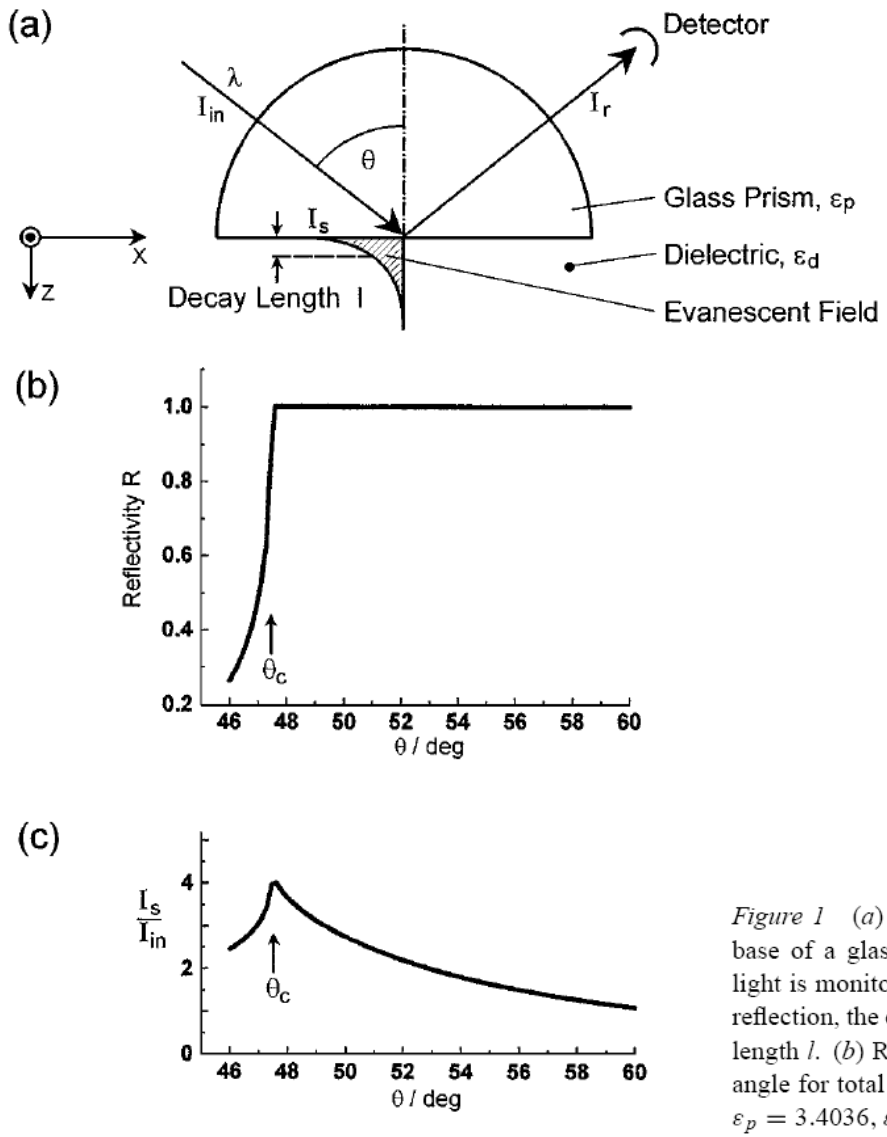

Figure 1 (*a*) Total internal reflection of a plane wave of wavelength λ and intensity I_{in} at the base of a glass prism with ε_p in contact with a dielectric medium of $\varepsilon_d < \varepsilon_p$. The reflected light is monitored with a detector. For incident angles $\theta > \theta_c$, the critical angle for total internal reflection, the evanescent field at the interface decays exponentially into the dielectric with a decay length l. (*b*) Reflectivity, i.e. I_r/I_{in}, as a function of the incident angle θ. θ_c denotes the critical angle for total internal reflection, and is given by $\sin\theta_c = \sqrt{\frac{\varepsilon_d}{\varepsilon_p}}$. The curve was calculated with $\varepsilon_p = 3.4036$, $\varepsilon_d = 1.778$. (*c*) Intensity enhancement, I_s/I_{in}, at the interface ($z = 0$) as a function of the incident angle θ.

We consider an interface in the xy-plane between two half-infinite spaces, 1 and 2, of materials the optical properties of which are described by their complex frequency-dependent dielectric functions $\tilde{\varepsilon}_1(\omega)$ and $\tilde{\varepsilon}_2(\omega)$, respectively. We ignore magnetic materials. Surface polaritons can only be excited at such an interface if the dielectric displacement $\vec{D}$ of the electromagnetic mode has a component normal to the surface ($\|\vec{z}$) which can induce a surface charge density σ,

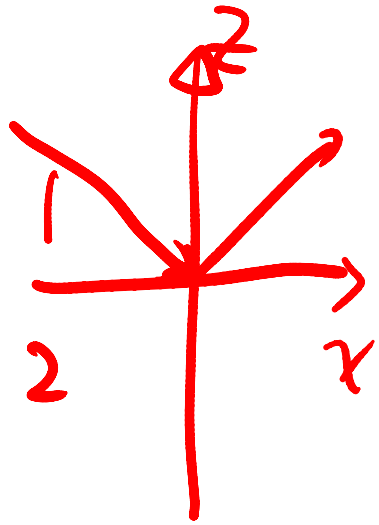

$$(\vec{D}_2 - \vec{D}_1) \cdot \vec{z} = 4\pi\sigma. \qquad 2.$$

S-polarized light propagating along the x-direction possesses only electric field components, $\vec{E}_i$, parallel to the surface (‖y-direction), i.e. transversal electric (TE) waves have $\vec{E}_i = (0, E_y, 0)$, and hence are unable to excite surface polaritons. Only p-polarized light (transversal magnetic TM) modes with $E = (E_x, 0, E_z)$, or, equivalently, $\vec{H} = (0, H_y, 0)$, can couple to such modes. The resulting surface electromagnetic wave, therefore, will have the following general form

$$\vec{A}_1 = \vec{A}_{10} e^{i(\vec{k}_{x1}\vec{x} + \vec{k}_{z1}\vec{z} - \omega t)} \text{ in medium } 1, z < 0 \qquad 3a.$$

and

$$\vec{A}_2 = \vec{A}_{20} e^{i(\vec{k}_{x2}\vec{x} - \vec{k}_{z2}\vec{z} - \omega t)} \text{ in medium } 2, z > 0, \qquad 3b.$$

where $\vec{A}$ stands for $\vec{E}$ and $\vec{H}$; $\vec{k}_{x1}$, and $\vec{k}_{x2}$ are the wavevectors in the x-direction; $\vec{k}_{z1}$, and $\vec{k}_{z2}$ those in the z-direction, i.e. normal to the interface; and ω is the angular frequency. Both fields $\vec{E}$ and $\vec{H}$ must fulfill the Maxwell equations:

$$\nabla \cdot \vec{H} = 0, \tag{4.}$$

$$\nabla \cdot \vec{E} = 0, \tag{5.}$$

$$\nabla \times \vec{E} + \frac{1}{c}\frac{\partial \vec{H}}{\partial t} = 0, \tag{6.}$$

$$\nabla \times \vec{H} - \frac{\varepsilon}{c}\frac{\partial \vec{E}}{\partial t} = 0, \tag{7.}$$

with c being the speed of light in vacuo and ε the dielectric function of the material. The tangential components of $\vec{E}$ and $\vec{H}$ have to be equal at the interface, i.e.

$$E_{x1} = E_{x2} \tag{8.}$$

and

$$H_{y1} = H_{y2}. \tag{9.}$$

From Equation 8 it follows immediately that $k_{x1} = k_{x2} = k_x$. On the other hand, it follows from Equations 3 and 7 that

$$k_{z1} H_{y1} = \frac{\omega}{c} \varepsilon_1 E_{x1} \tag{10.}$$

and

$$k_{z2} H_{y2} = -\frac{\omega}{c} \varepsilon_2 E_{x2}. \tag{11.}$$

This leads to the only nontrivial solution if:

$$\frac{k_{z1}}{k_{z2}} = -\frac{\varepsilon_1}{\varepsilon_2}. \tag{12.}$$

Equation 12 indicates that surface electromagnetic modes can only be excited at interfaces between two media with dielectric constants of opposite sign.

Here we are dealing with the interface between a metal with its complex dielectric function ($\tilde{\varepsilon}_m = \varepsilon'_m + i\varepsilon''_m$) and a dielectric material ($\tilde{\varepsilon}_d = \varepsilon'_d + i\varepsilon''_d$), hence, with coupling the collective plasma oscillations of the nearly free electron gas in a metal to an electromagnetic field (5). These excitations are called plasmon surface polaritons (PSP) or surface plasmons, for short. From Equations 6, 7, 10, and 11 we obtain

$$k_x^2 + k_{zd}^2 = \left(\frac{\omega}{c}\right)^2 \varepsilon_d \qquad 13.$$

or

$$k_{zd} = \sqrt{\varepsilon_d \left(\frac{\omega}{c}\right)^2 - k_x^2}. \qquad 14.$$

With Equation 12 this leads to the dispersion relationships (i.e. the energy-momentum relation) for surface plasmons at a metal/dielectric interface:

$$k_x = \frac{\omega}{c}\sqrt{\frac{\varepsilon_m \cdot \varepsilon_d}{(\varepsilon_m + \varepsilon_d)}}. \qquad 15.$$

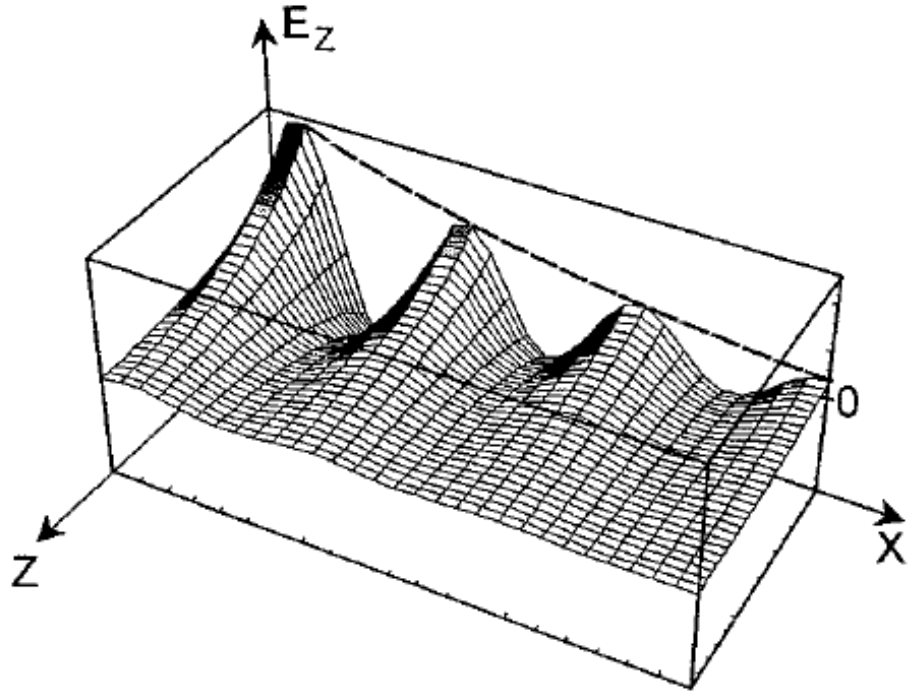

Figure 2 Schematic of the evanescent character of a surface plasmon mode excited at a metal/dielectric interface in the x-, y-plane propagating as a damped oscillatory wave in the x-direction. The electric field components along the z-direction, normal to the interface, decay exponentially, here shown for the E_z component.

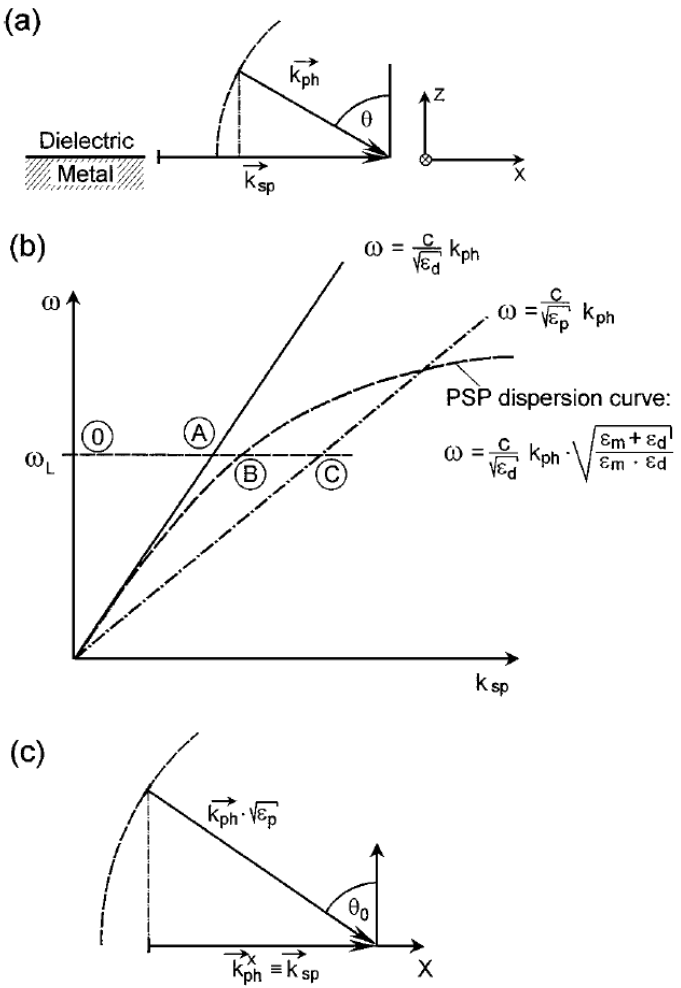

Figure 3 (*a*) Momentum relation between a surface plasmon, $\vec{k}_{sp}$, propagating along x and a photon, $\vec{k}_{ph}$, incident at the metal/dielectric interface at an angle θ. At any angles θ, $|\vec{k}_{ph}| < |\vec{k}_{sp}|$. (*b*) Dispersion relation of a photon traveling as a plane wave in the dielectric medium, $\omega = c_d k_{ph}$, with $c_d = \frac{c}{\sqrt{\varepsilon_d}}$ the speed of light in the dielectric (*full line*), and of a photon propagating in the prism, $\omega = c_p k_{ph}$, $c_p = \frac{c}{\sqrt{\varepsilon_p}}$, *dash-dotted line. Dashed curve*, dispersion of the surface plasmon mode propagating along the metal/dielectric interface. The meaning of 0, A, B, and C is given in the text. (*c*) Wavevector matching condition for the resonant coupling of photons traveling in the prism: At the incident angle θ_0, the photon projection along the x-coordinate, $\vec{k}^x_{ph}$, matches the PSP wavevector $\vec{k}_{sp}$. For details, see text.

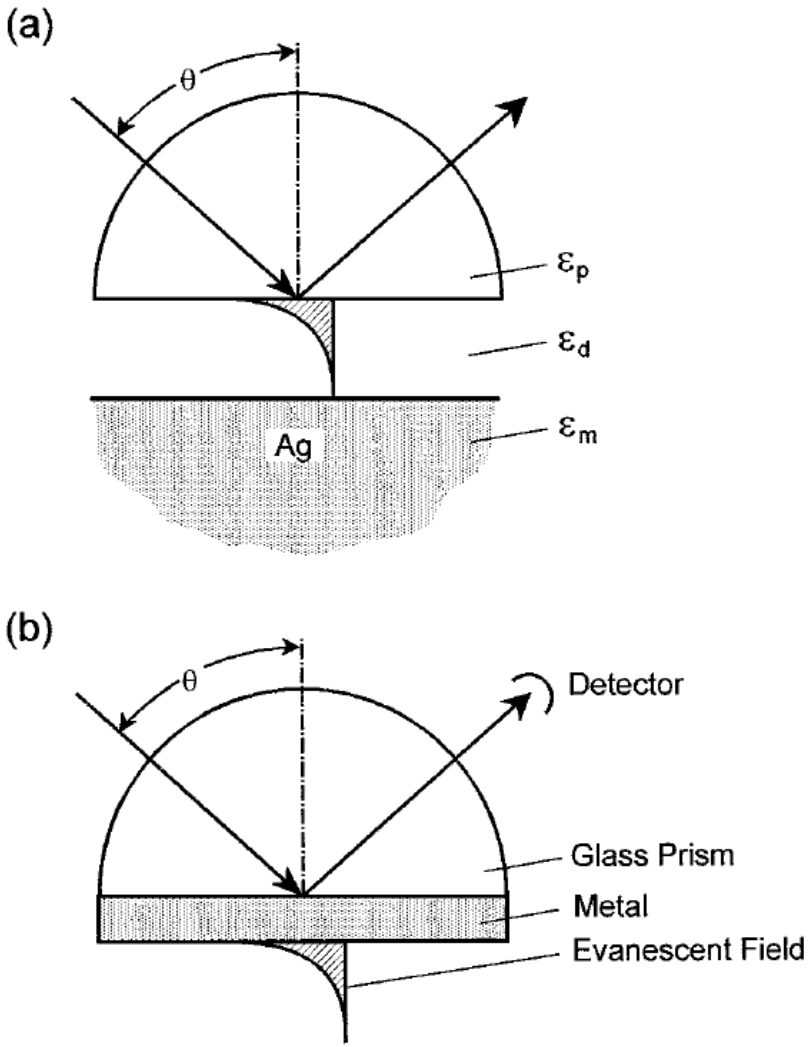

Figure 4 (*a*) The Otto configuration is based on the total internal reflection of a plane wave incident at an angle θ at the base of a prism. The evanescent tail of this inhomogeneous wave can excite PSP states at an Ag-dielectric interface, provided the coupling gap is sufficiently narrow. (*b*) Attenuated total internal reflection (ATR) construct for PSP excitation in the Kretschmann geometry. A thin metal film ($d \sim 50$ nm) is evaporated onto the base of the prism and acts as a resonator driven by the photon field incident at an angle θ.

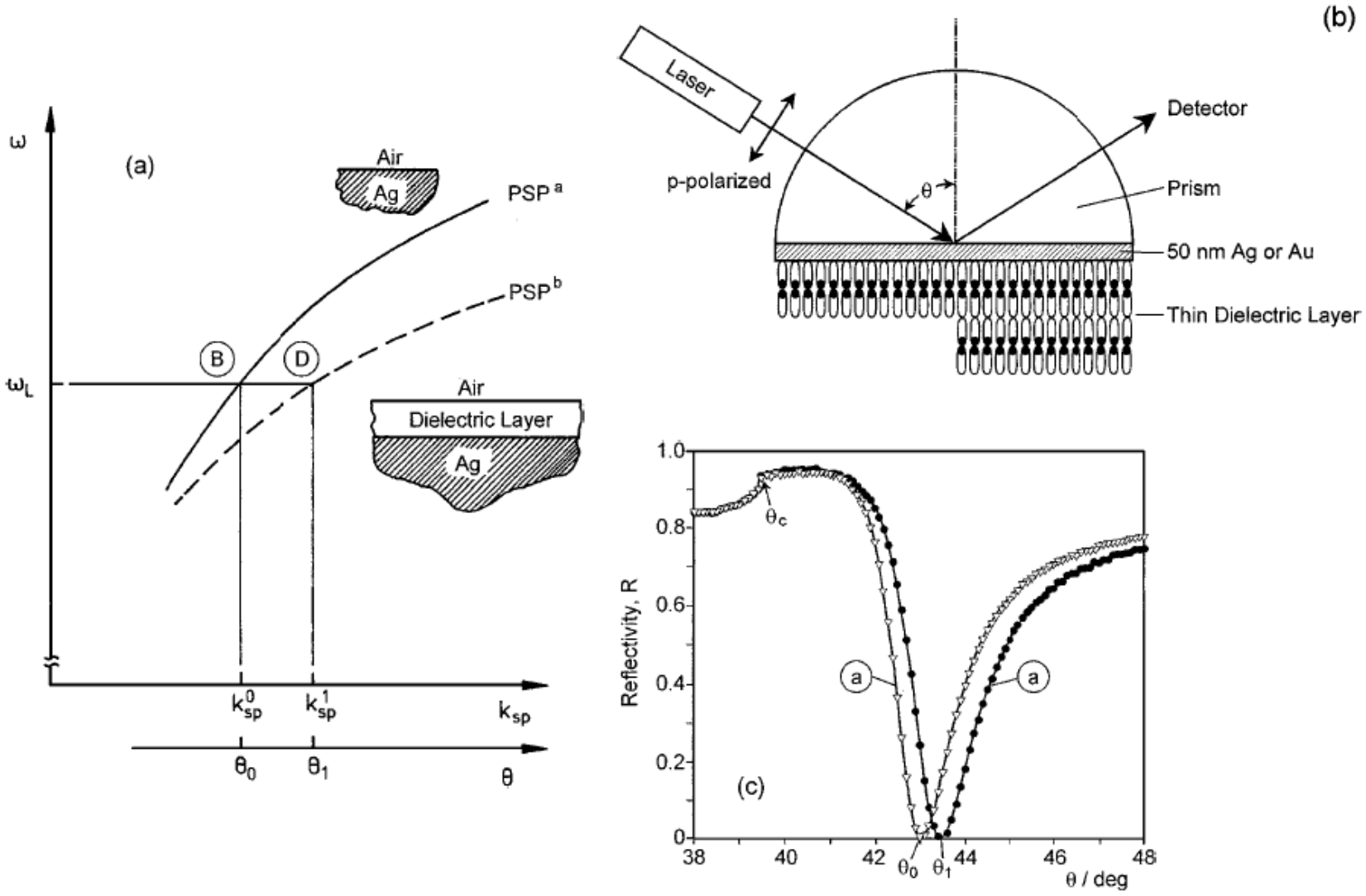

after self-assembling a monomolecular layer of HS-$(CH_2)_{21}$-OH. The symbols are experimental data points; the full curves are Fresnel fits with $\varepsilon_{BK7} = 2.29$, $\tilde{\varepsilon}_{Au} = -12.45 + i \cdot 1.3$, $d_{Au} = 46.9$ nm, $\varepsilon_{layer} = 2.1025$, $d_{layer} = 2.65$ nm. Data were taken at $\lambda = 633$ nm in air.

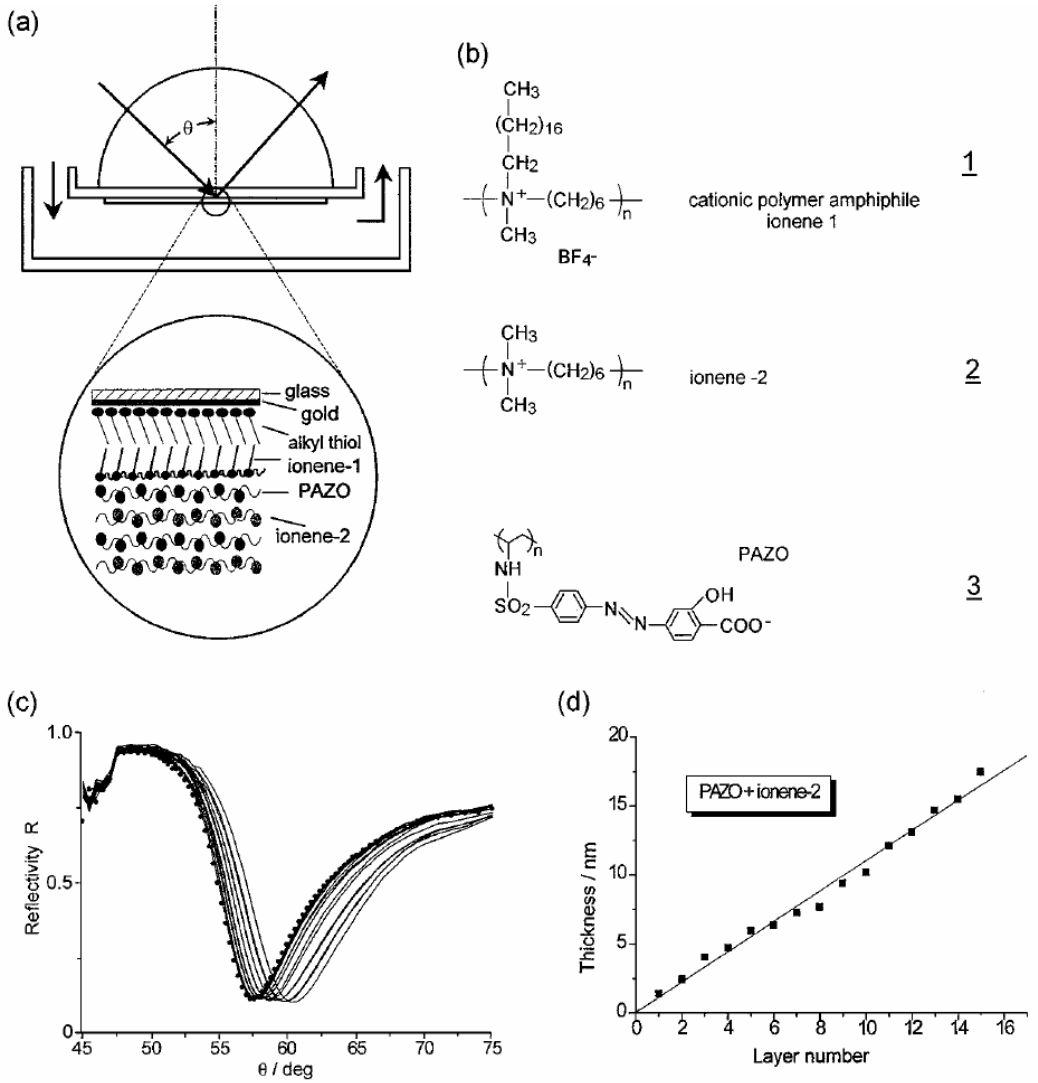

Figure 14 (*a*) Experimental construct for on-line surface plasmon optical observation of the alternating deposition of cationic and anionic polymers from solution to an Au substrate precoated by an alkyl thiol and an ionene-1 monolayer [refer to (*b*)]. The build-up architecture is given in the enlargement. (*b*) Structural formulas of the employed materials. (*c*) Series of ATR scans taken after each polyelectrolyte monolayer deposition. (*d*) Thickness increase as obtained from the ATR scans given in (*c*).

Glass Surface Modification

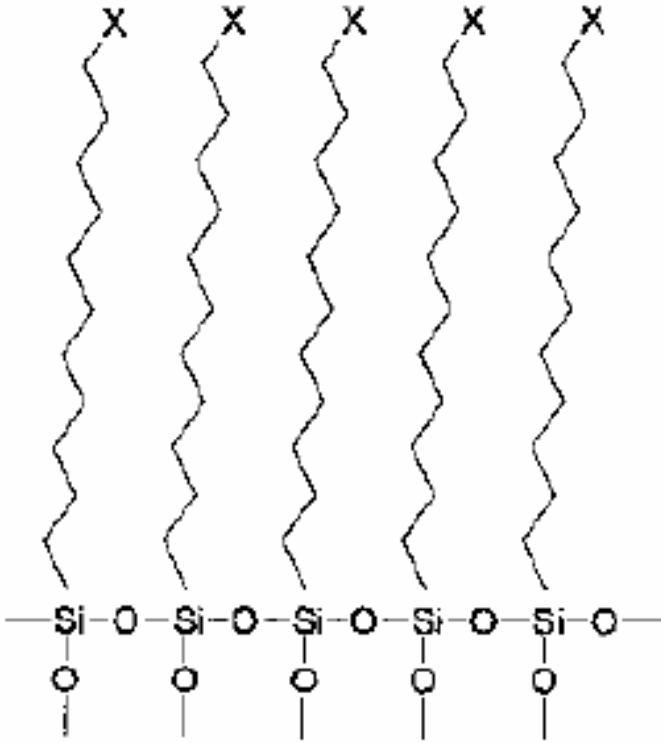

Hydroxylated Glass Surface

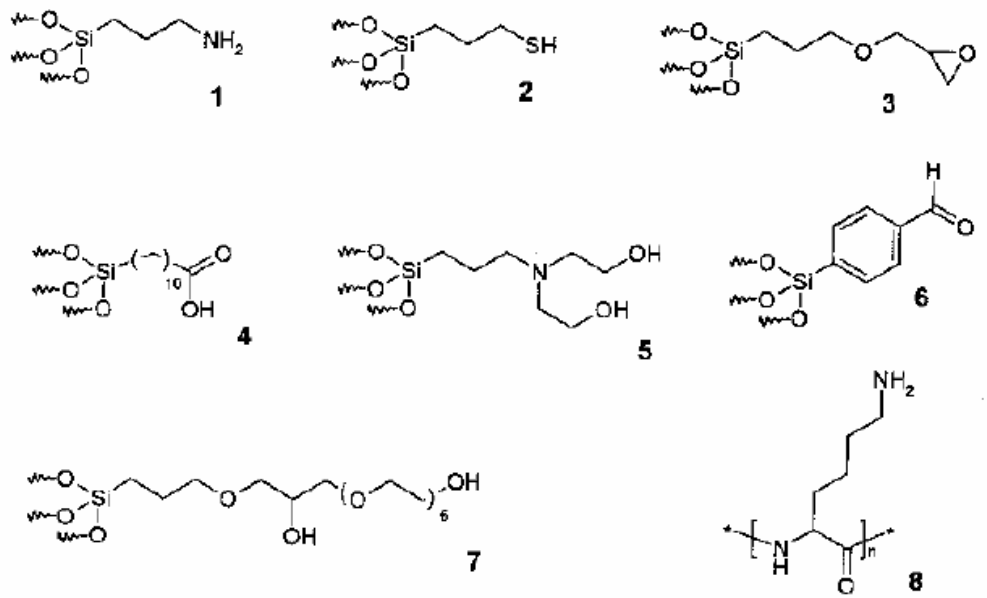

Scheme 2.2 Reagents for derivatization of glass surfaces. 1 APTES = aminopropyltriethoxysilane; **2** MPTS = 3-mercaptopropyltrimethoxysilane; **3** GPTS = glycidoxypropyltrimethoxysilane; **4** TETU = triethoxysilane undecanoic acid; **5** HE-APTS = bis(hydroxyethyl)aminopropyltriethoxysilane); **6** 4-trimethoxysilylbenzaldehyde; **7** GPTS/HEG = glycidoxypropyltrimethoxysilane-hexaethylene glycol; **8** poly(lysine).

Scheme 2.1 2D schematic description of a polysiloxane monolayer on a glass surface (X = terminal functional

Gold Surface Modification

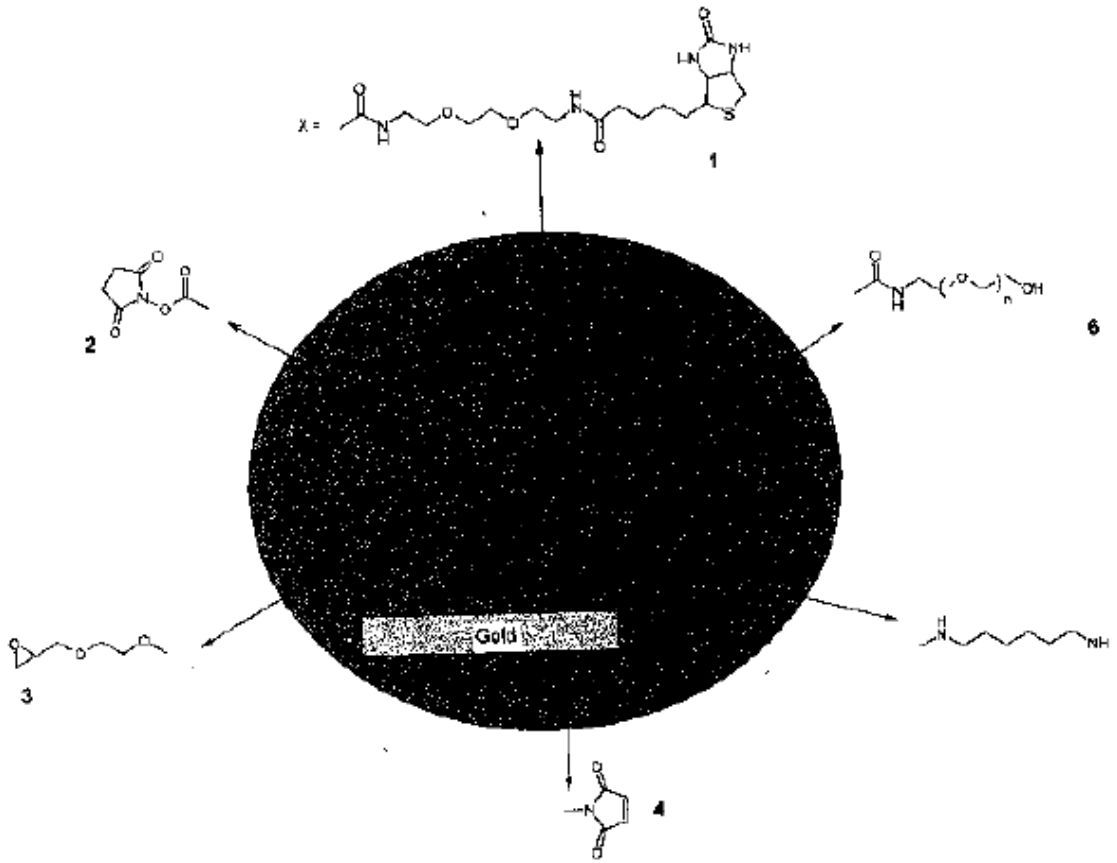

Scheme 2.3 Schematic respresentation of long-chain alkanethiol monolayers (e.g. 16 mercapto-hexadecanoic acid) on gold with different terminal functional groups.

1, biotin; 2, NHS-ester (NHS, N-hydroxysuccin-imide); 3, epoxy-ethylene glycol;
4, maleimide; 5, diaminohexane; 6 oligo (ethylene glycol).

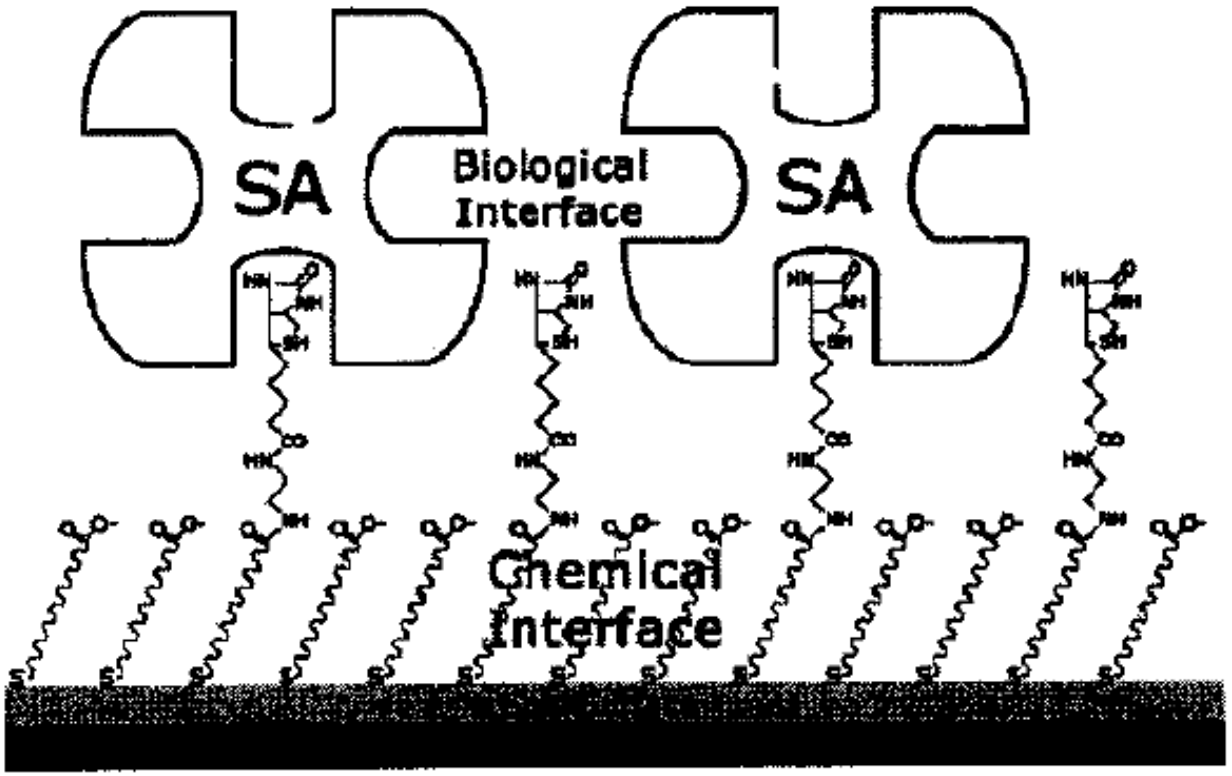

Figure 2.3 Schematic respresentation of a steptavidin sensor surface assembled on a reaction-controlled biotinylated SAM [28].

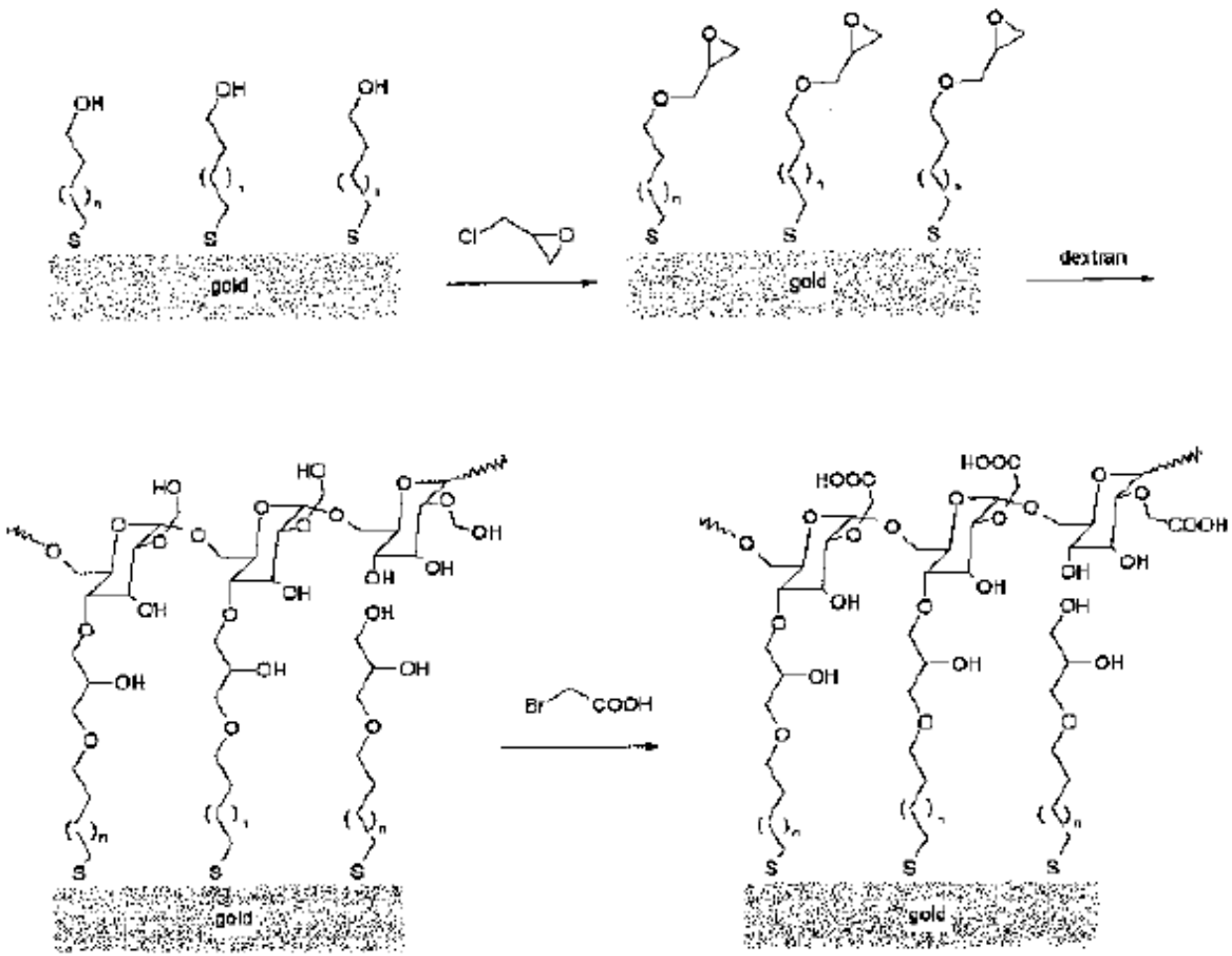

Scheme 2.4 Reaction schemes for preparing a hydrogel dextran matrix [41].

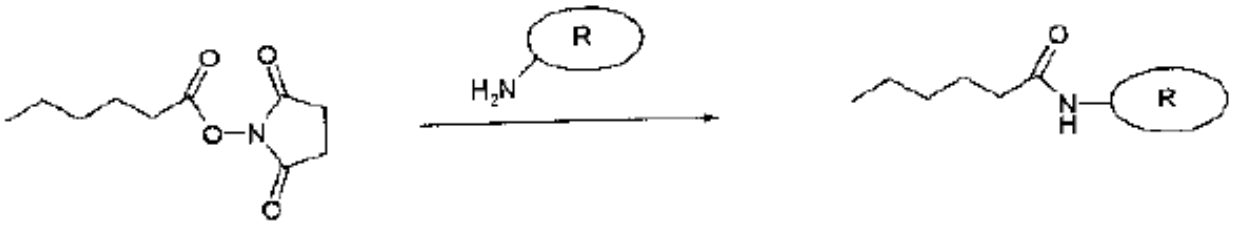

Scheme 2.6 Surface coupling reaction of NHS-esters with the amino residues of the side-chains of polypeptides (lysine units). R, protein.

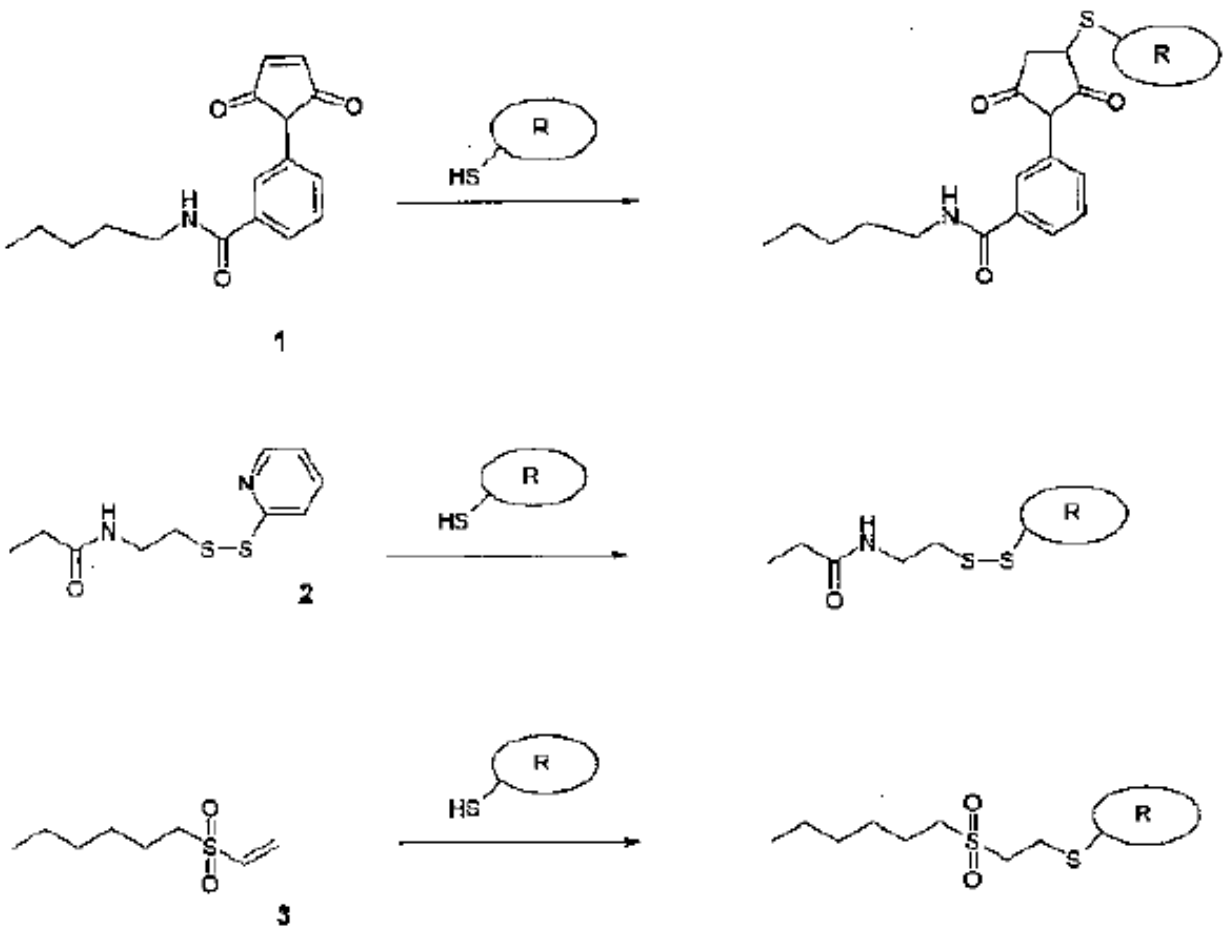

Scheme 2.7 Surface modifications for the attachment of thiol residues (which are present in the side chains) of polypeptides (cysteine units). R, protein, **1**, maleimide; **2**, disulfides; 3, vinyl sulfone.

his tag

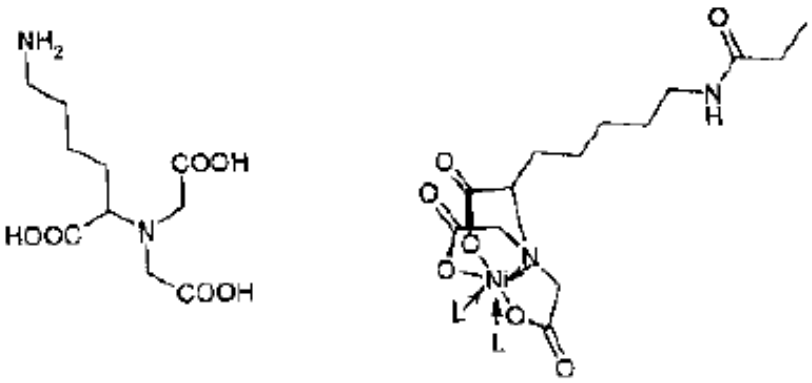

A B

Scheme 2.12 (A) Structure of N-(5-amino-1-carboxypentyl)iminodiacetic acid. (B) The quadridentate nitrilotriacetic acid (NTA) ligand forms a complex with four binding sites on the nickel metal which is present in the center. The two remaining binding sites can be coordinated with histidine ligands (L).

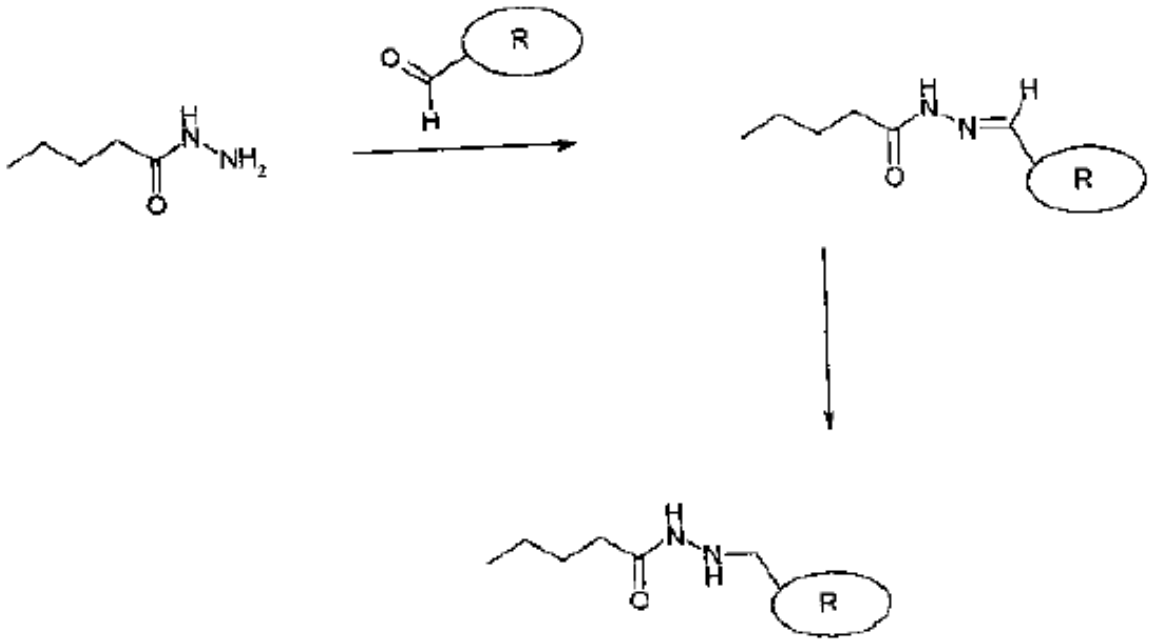

Scheme 2.13 Coupling of aldehyde residues of glycoproteins to hydrazide-terminated monolayers.

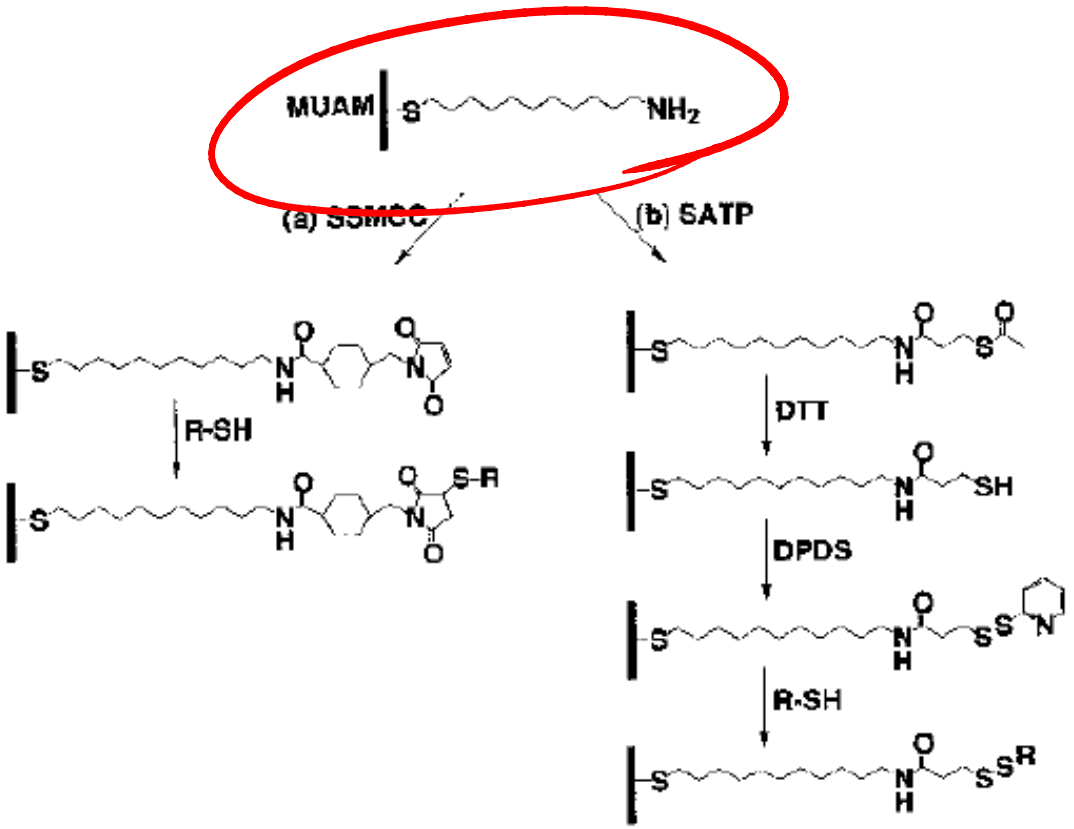

Figure 5.3 Surface attachment chemistry for the immobilization of thiol-modified DNA and cysteine-containing peptides: (a) The linker SSMCC is reacted with a well-packed self-assembled monolayer of 11-mercaptoundecylamine (MUAM) to create a maleimide-modified surface. The maleimide surface is then used to covalently attach thiol-modified DNA or cysteine-containing peptides. (b) In the second approach, SATP is reacted with MUAM to create a protected thiol surface. Upon deprotection with a basic solution containing DTT, the free sulfhydryl is reacted with dipyridyl disulfide to create a pyridyl disulfide surface. Thiol–disulfide exchange reactions are used to couple thiol-containing biomolecules to the surface.

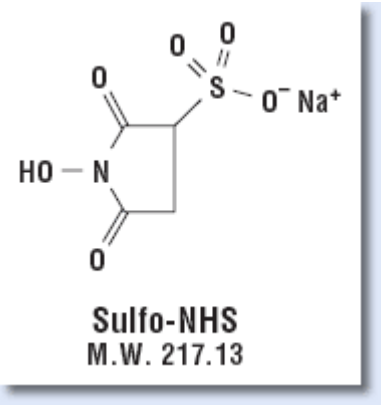

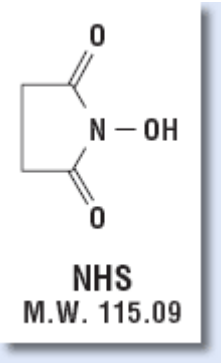

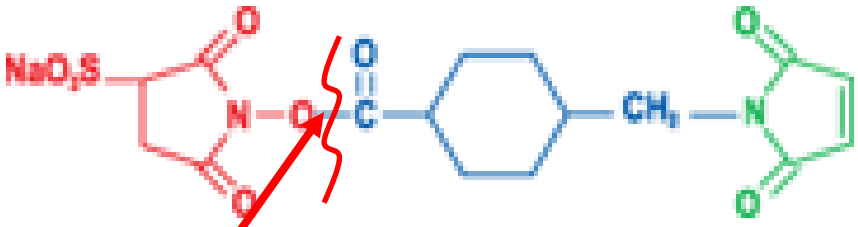

SulfoSuccinimidyl-4-(N-Maleimidomethyl)Cyclohexane-1-Carboxylate
SSMCC

The most popular NH_2- and SH- crosslinker

N-hydroxysuccinimide

NH_2 => amide

$R_1NH_2 + NHS\text{-}R_2 = >R_1NHC{=}OR_2$

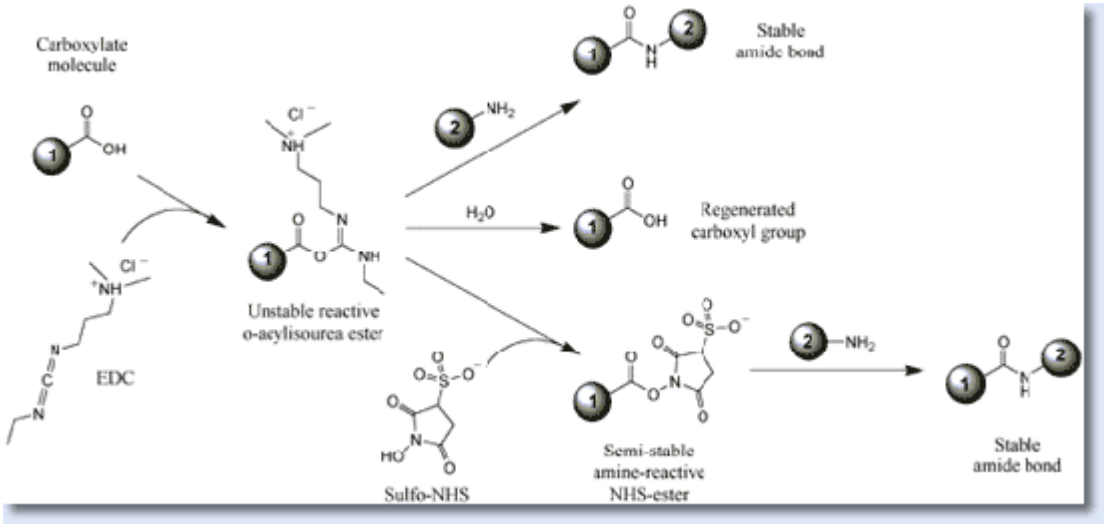

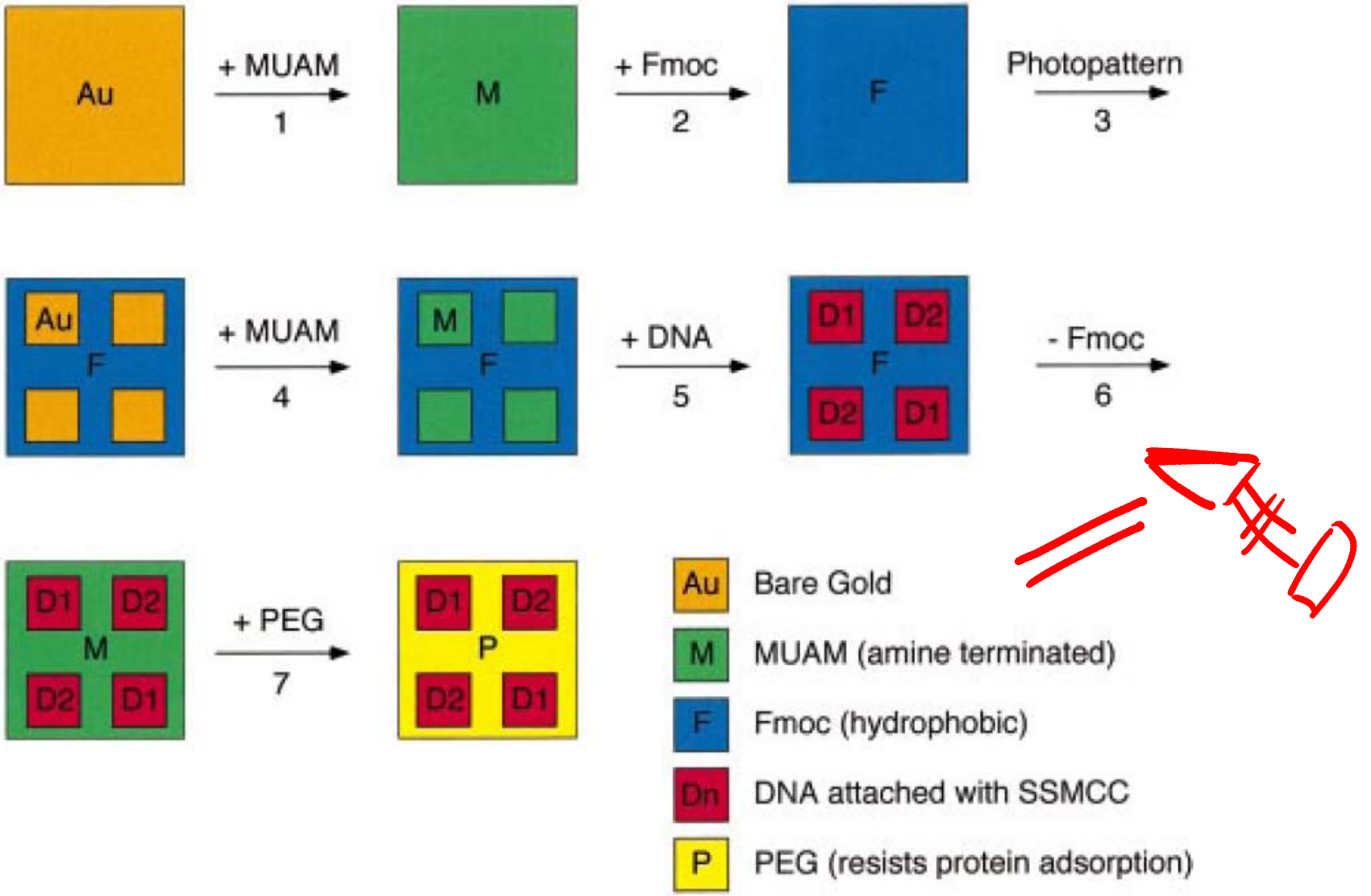

Figure 1. Fabrication scheme for the construction of multi-element DNA arrays. A clean gold surface is reacted with the amine-terminated alkanethiol MUAM, and subsequently reacted with Fmoc-NHS to create a hydrophobic surface. This surface is then exposed to UV radiation through a quartz mask and rinsed with solvent to remove the MUAM+Fmoc from specific areas of the surface, leaving bare gold pads. These bare gold areas on the sample surface are filled in with MUAM, resulting in an array of MUAM pads surrounded by a hydrophobic Fmoc background. Solutions of DNA are then delivered by pipet onto the specific array locations and are covalently bound to the surface via the bifunctional linker SSMCC. In the final two steps, the Fmoc-terminal groups on the array background are removed and replaced by PEG groups which prohibit the nonspecific binding of analyte proteins to the background.

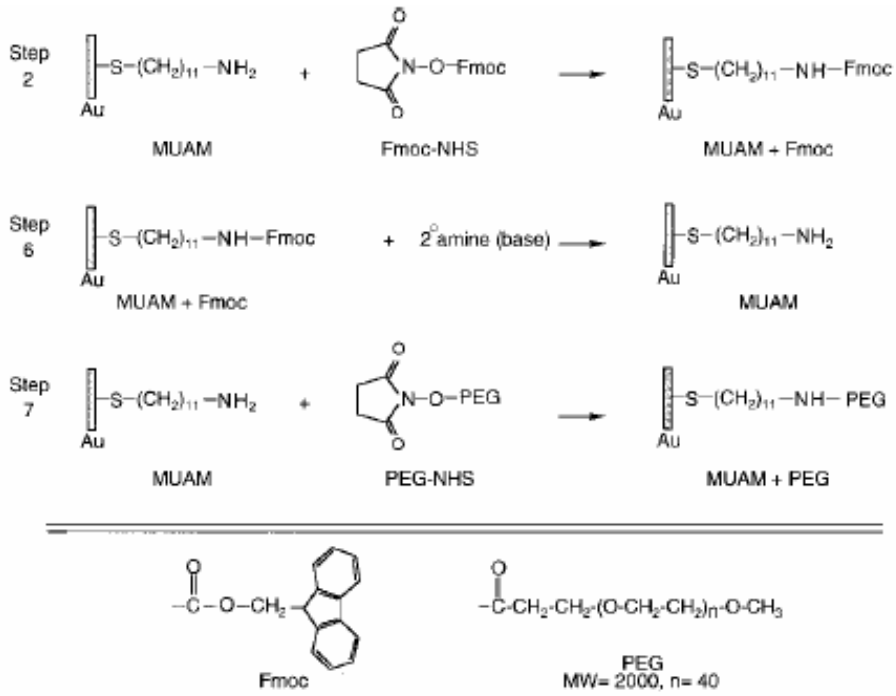

Figure 2. Surface reaction scheme showing the steps involved in the reversible modification of the array background. (Step 2) The starting amine-terminated alkanethiol surface (MUAM) is reacted with the Fmoc-NHS protecting group to form a carbamate linkage thus creating a hydrophobic Fmoc-terminated surface. (Step 6) After DNA immobilization (see Figure 3), the hydrophobic Fmoc group is removed from the surface with a basic secondary amine, resulting in the return of the original MUAM surface. (Step 7) In the final array fabrication step, the deprotected MUAM is reacted with PEG-NHS to form an amide bond that covalently attaches PEG to the array surface.

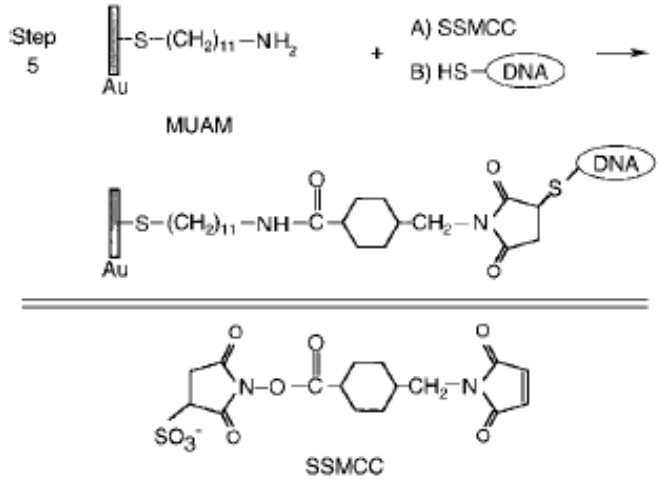

Figure 3. Surface reaction scheme showing the immobilization of thiol-terminated DNA to the array surface. In Step 5 of the DNA array fabrication, the heterobifunctional linker SSMCC is used to attach 5′-thiol modified oligonucleotide sequences to reactive pads of MUAM. This linker contains an NHSS ester functionality (reactive toward amines) and a maleimide functionality (reactive toward thiols). The surface is first exposed to a solution of the linker, whereby the NHSS ester end of the molecule reacts with the MUAM surface. Excess linker is rinsed away and the array surface is then spotted with 5′-thiol-modified DNA that reacts with the maleimide groups forming a covalent bond to the surface monolayer.

Probing Single Molecules and Single Nanoparticles by Surface-Enhanced Raman Scattering

SCIENCE • VOL. 275 • 21 FEBRUARY 1997

Shuming Nie* and Steven R. Emory

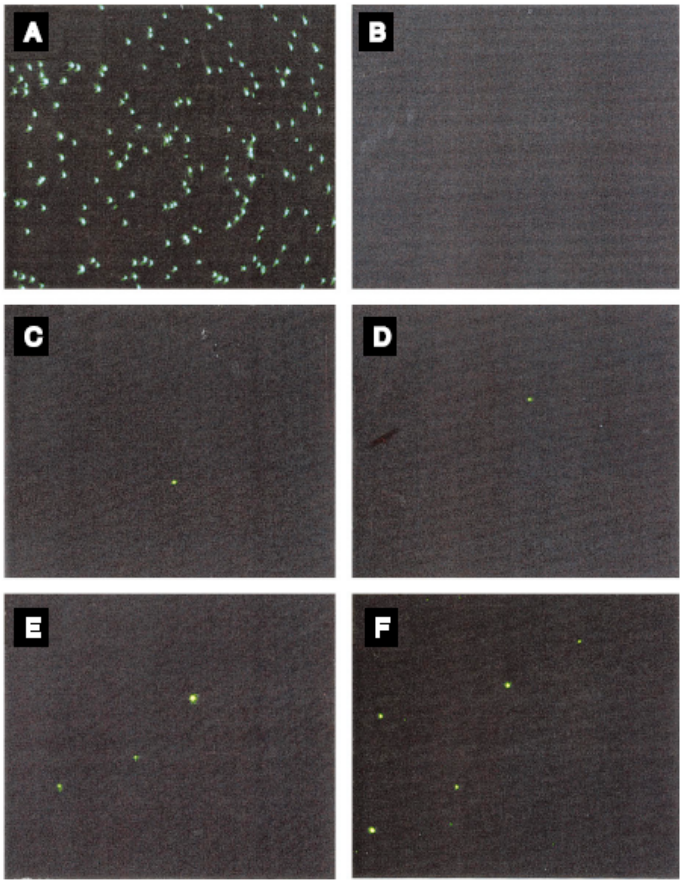

Fig. 1. Single Ag nanoparticles imaged with evanescent-wave excitation. Total internal reflection of the laser beam at the glass-liquid interface was used to reduce the laser scattering background. The instrument setup for evanescent-wave microscopy was adapted from Funatsu *et al.* (*11*). The images were directly recorded on color photographic film (ASA-1600) with a 30-s exposure by a Nikon 35-mm camera attached to the microscope. (**A**) Unfiltered photograph showing scattered laser light from all particles immobilized on a polylysine-coated surface. (**B**) Filtered photographs taken from a blank Ag colloid sample (incubated with 1 mM NaCl and no R6G analyte molecules). (**C**) and (**D**) Filtered photographs taken from a Ag colloid sample incubated with 2×10^{-11} M R6G. These images were selected to show at least one Raman scattering particle. Different areas of the cover slip were rapidly screened, and most fields of view did not contain visible particles. (**E**) Filtered photograph taken from Ag colloid incubated with 2×10^{-10} M R6G. (**F**) Filtered photograph taken from Ag colloid incubated with 2×10^{-9} M R6G. A high-performance bandpass filter was used to remove the scattered laser light and to pass Stokes-shifted Raman signals from 540 to 580 nm (920 to 2200 cm^{-1}). Continuous-wave excitation at 514.5 nm was provided by an Ar ion laser. The total laser power at the sample was 10 mW. Note the color differences between the scattered laser light in (A) and the red-shifted light in (C) through (F).

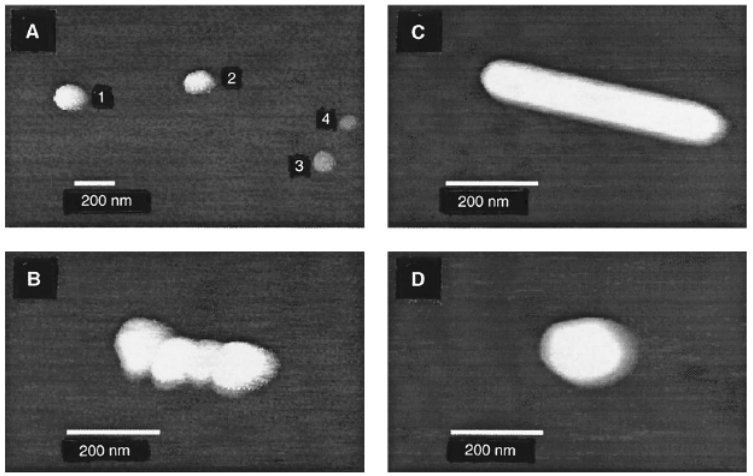

Fig. 2. Tapping-mode AFM images of screened Ag nanoparticles. (**A**) Large area survey image showing four single nanoparticles. Particles 1 and 2 were highly efficient for Raman enhancement, but particles 3 and 4 (smaller in size) were not. (**B**) Close-up image of a hot aggregate containing four linearly arranged particles. (**C**) Close-up image of a rod-shaped hot particle. (**D**) Close-up image of a faceted hot particle.

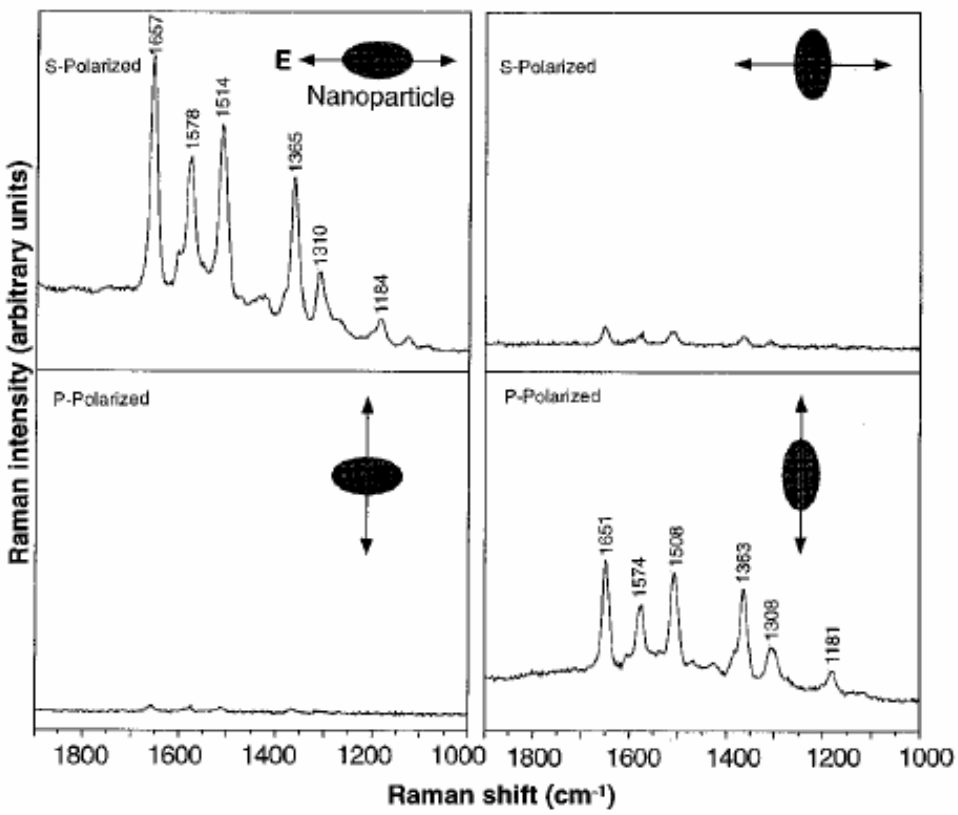

Fig. 3. Surface-enhanced Raman spectra of R6G obtained with a linearly polarized confocal laser beam from two Ag nanoparticles. The R6G concentration was 2×10^{-11} M, corresponding to an average of 0.1 analyte molecule per particle. The direction of laser polarization and the expected particle orientation are shown schematically for each spectrum. Laser wavelength, 514.5 nm; laser power, 250 nW; laser focal radius, ~250 nm; integration time, 30 s. All spectra were plotted on the same intensity scale in arbitrary units of the CCD detector readout signal.

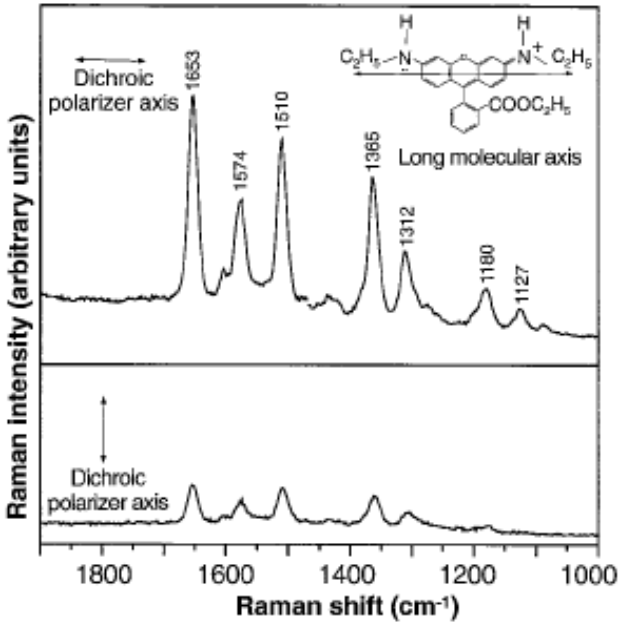

Fig. 4. Emission-polarized surface-enhanced Raman signals of R6G observed from a single Ag nanoparticle with a polarization-scrambled confocal laser beam. A dichroic sheet polarizer was rotated 90° to select Raman scattering signals polarized parallel (upper spectrum) or perpendicular (lower spectrum) to the long molecular axis of R6G. (**Inserts**) Structure of R6G, the electronic transition dipole (along the long axis when excited at 514.5 nm), and the dichroic polarizer orientations. Other conditions as in Fig. 3.

troscopic signatures of adsorbed molecules. For single rhodamine 6G molecules adsorbed on the selected nanoparticles, the intrinsic Raman enhancement factors were on the order of 10^{14} to 10^{15}, much larger than the ensemble-averaged values derived from conventional measurements. This enormous enhancement leads to vibrational Raman signals that are more intense and more stable than single-molecule fluorescence.

Electromagnetic contributions to single-molecule sensitivity in surface-enhanced Raman scattering

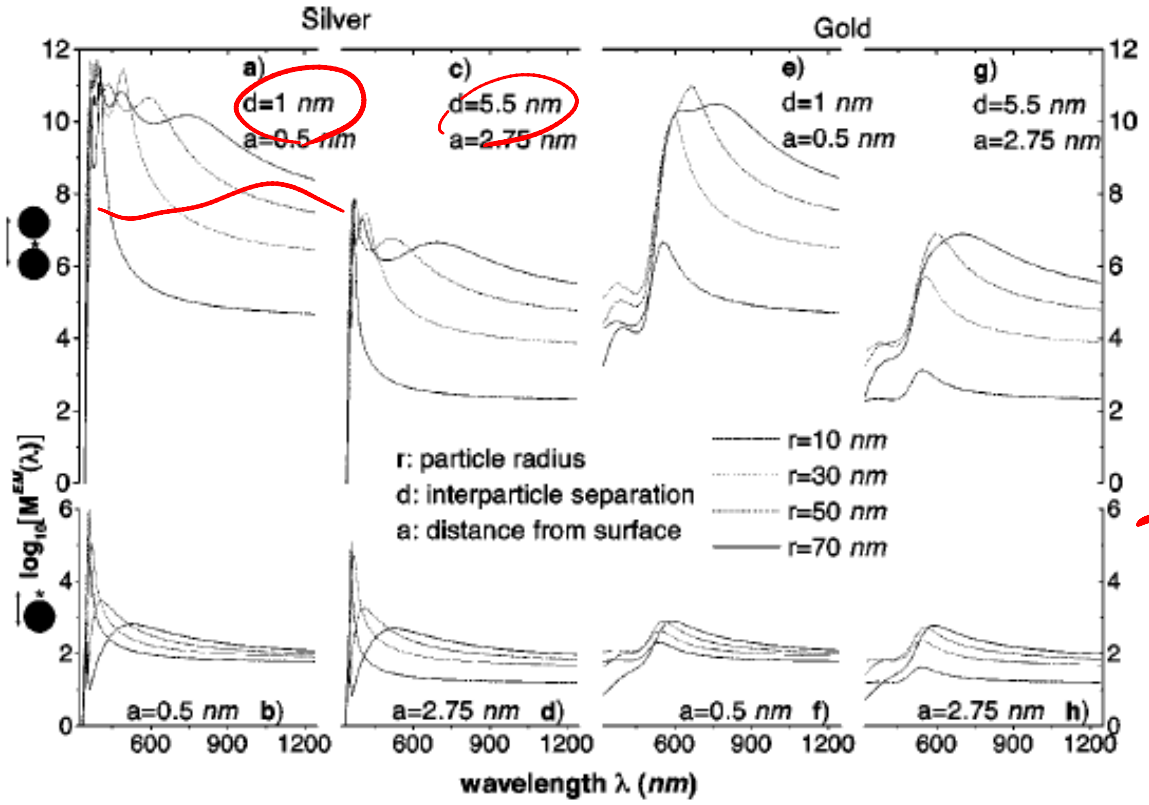

Chemical
$10 \sim 10^2$

EM
$10^3 \sim 10^4$

$10^4 \sim 10^6$

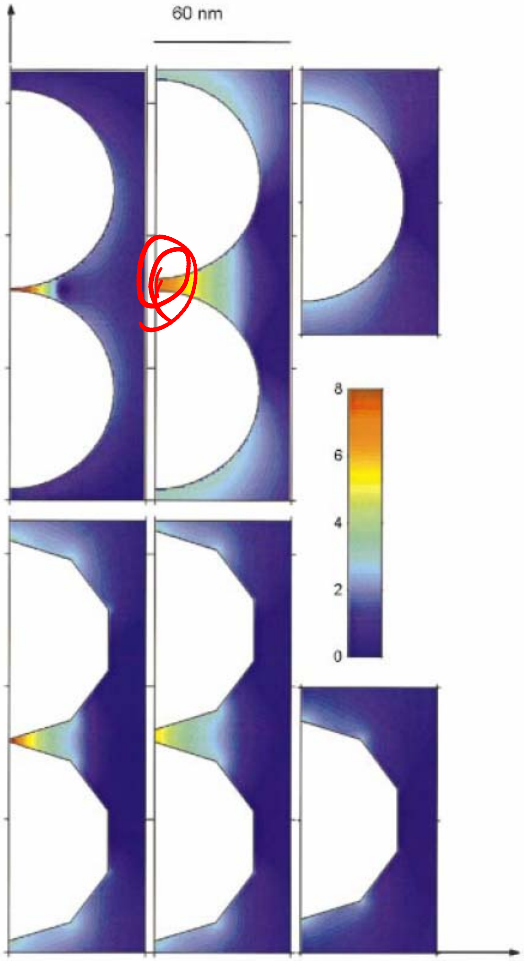

FIG. 3. (Color) EM-enhancement factor M^{EM} at a cross section through six different silver particle configurations. The wavelength of the incident field is $\lambda = 514.5$ nm with vertical polarization. The left-hand column illustrates the EM enhancement for dimer configurations of two spheres (top) and two polygons (bottom) with a separation of 1 nm. The middle column shows the same situation, but with a separation distance of 5.5 nm. The right-hand column shows the case of an isolated single particle. All particles share a common largest dimension of 90 nm. Note that the color scale from dark blue to dark red is logarithmic, covering the interval $10^0 < M^{EM} < 10^8$. Regions with enhancement outside this interval are shown in dark blue and dark red, respectively.

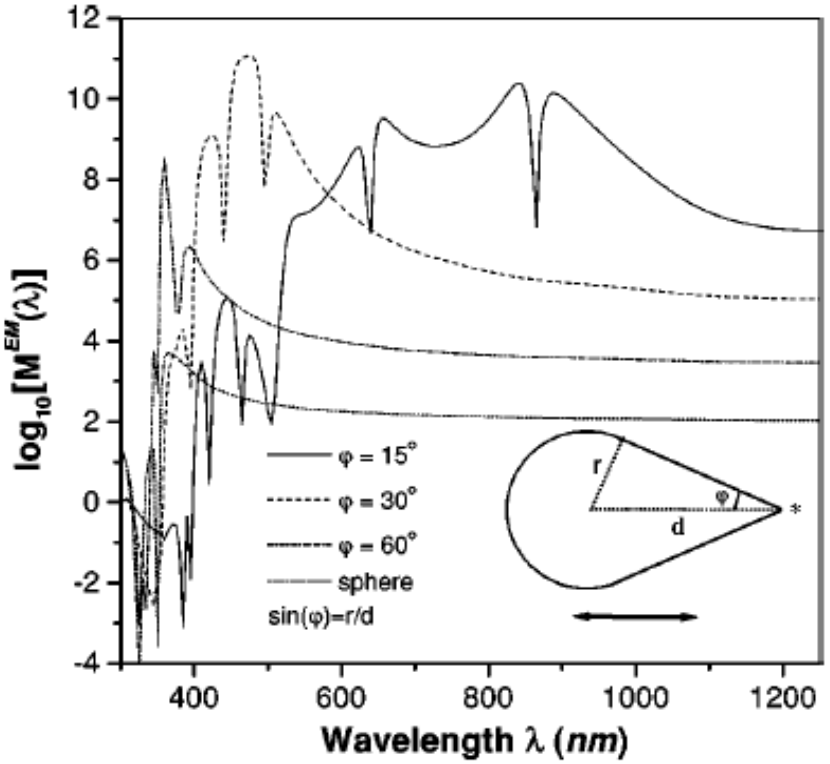

FIG. 5. EM-enhancement factor for a rotationally symmetric silver droplet as a function of the angle defining the opening edge ϕ. The field is polarized parallel to the axis of the droplet and the evaluation position (star) is located 0.5 nm outside the tip. As the droplet becomes sharper the enhancement increases several orders of magnitude.

Drift: Drude model

$$F = ma$$

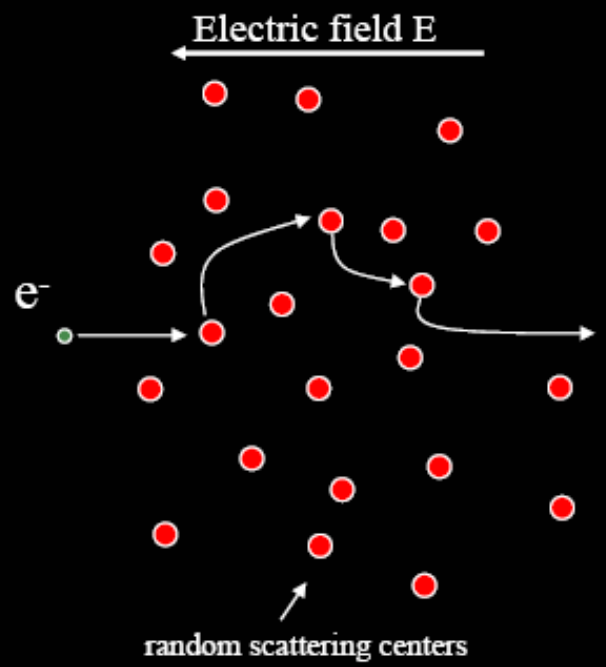

Drift: Drude model

$$F = ma$$

$$eE = m \frac{\partial v}{\partial t}$$

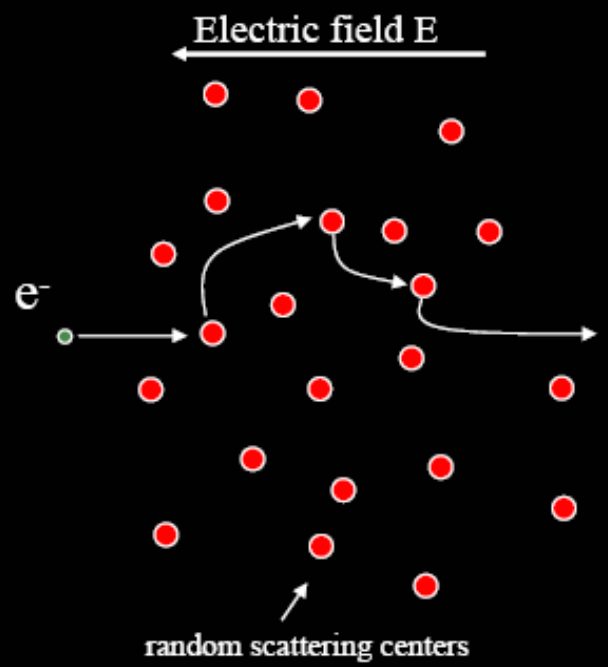

Drift: Drude model

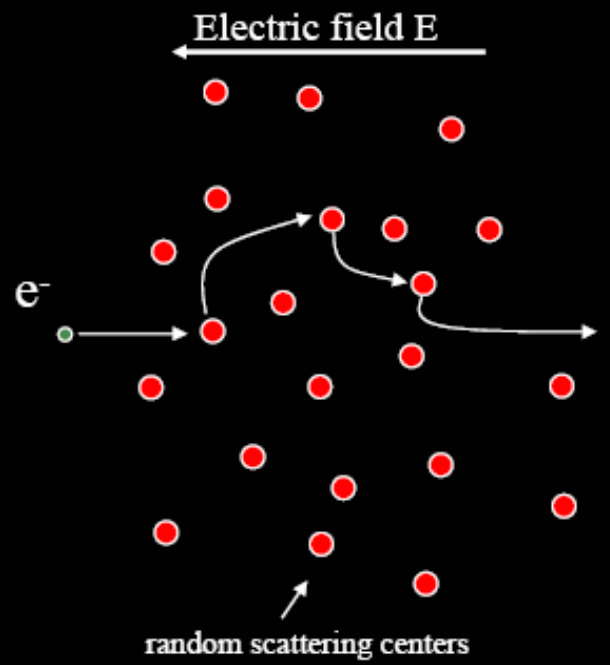

$$F = ma$$

$$eE = m \frac{\partial v}{\partial t}$$

$$v_{avg} = \frac{e\tau}{m} E$$

Drift: Drude model

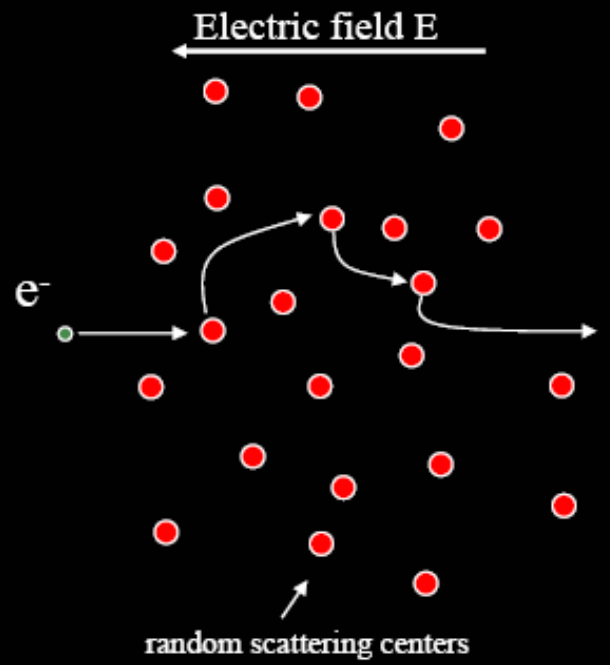

$$F = ma$$

$$eE = m\frac{\partial v}{\partial t}$$

$$v_{avg} = \underbrace{\frac{e\tau}{m}}_{\mu} E$$

Drift: Drude model

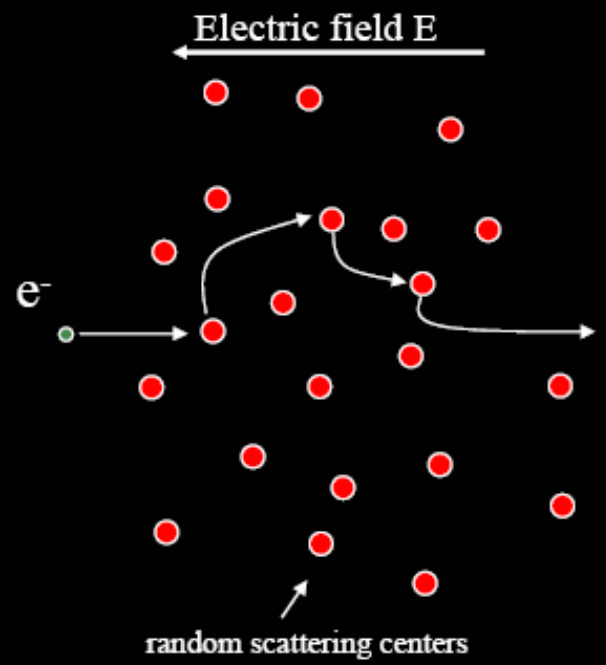

$$F = ma$$

$$eE = m\frac{\partial v}{\partial t}$$

$$v_{avg} = \underbrace{\frac{e\tau}{m}}_{\mu} E$$

$$j = nev_{avg} = \frac{ne^2\tau}{m}E$$

Drift: Drude model

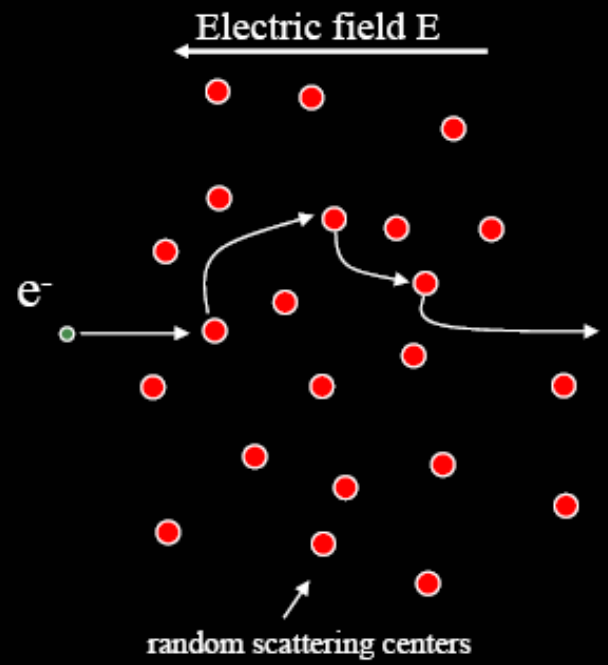

$$F = ma$$

$$eE = m\frac{\partial v}{\partial t}$$

$$v_{avg} = \underbrace{\frac{e\tau}{m}}_{\mu} E$$

$$j = nev_{avg} = \underbrace{\frac{ne^2\tau}{m}}_{\sigma} E$$

$$m\frac{\partial}{\partial t}\langle\vec{v}\rangle = q\vec{E} - \gamma\langle\vec{v}\rangle$$

$$\sigma(\omega) = \frac{\sigma_0}{1 + i\omega\tau}$$

Types of scattering

- Electron-phonon:
  - Very temperature dependent
  - Phonons are lattice vibrations
  - At low temperatures, lattice is "perfectly still"
- Impurity scattering
  - Temperature independent
  - Depends on impurity concentration